Research article

JGS
Journal of the Geological Society

Published Online First

https://doi.org/10.1144/jgs2018-097

Fossil biomass preserved as graphitic carbon in a late Paleoproterozoic banded iron formation metamorphosed at more than 550°C

Dominic Papineau[1,2,3]*, Bradley T. De Gregorio[4], James Sagar[1], Richard Thorogate[1], Jianhua Wang[5], Larry Nittler[5], David A. Kilcoyne[6], Hubertus Marbach[7], Martin Drost[7] & Geoff Thornton[1,8]

[1] London Centre for Nanotechnology, University College London, 17–19 Gordon Street, London, WC1H 0AH UK
[2] Department of Earth Sciences, University College London, London, WC1E 6BS UK
[3] Centre for Planetary Sciences, UCL-Birkbeck, London, WC1E 6BT UK
[4] Materials Science and Technology Division, US Naval Research Laboratory, Washington, DC 20375-5320, USA
[5] Department of Terrestrial Magnetism, Carnegie Institution for Science, Washington, DC 20015, USA
[6] Advanced Light Source, Lawrence Berkeley National Laboratory, Berkeley, CA 94720, USA
[7] Microscopy and Nanolithography Group, Lehrstuhl für Physikalische Chemie II, Friedrich-Alexander-Universität Erlangen–Nürnberg, Erlangen, 91058 Germany
[8] Department of Chemistry, University College London, 20 Gordon Street, London, WC1E 6BT UK

D.P., 0000-0003-0063-7514; B.T.D., 0000-0001-9096-3545; L.N., 0000-0002-5292-6089; D.A.K., 0000-0002-8805-8690; G.T., 0000-0002-1616-5606

*Correspondence: d.papineau@ucl.ac.uk

Abstract: Metamorphism is thought to destroy microfossils, partly through devolatilization and graphitization of biogenic organic matter. However, the extent to which there is a loss of molecular, elemental and isotope signatures from biomass during high-temperature metamorphism is not clearly established. We report on graphitic structures inside and coating apatite grains from the *c.* 1850 Ma Michigamme silicate banded iron formation from Michigan, metamorphosed above 550°C. Traces of N, S, O, H, Ca and Fe are preserved in this graphitic carbon and X-ray spectra show traces of aliphatic groups. Graphitic carbon has an expanded lattice around 3.6 Å, forms microscopic concentrically-layered and radiating polygonal flakes and has homogeneous $\delta^{13}C$ values around −22‰, identical to bulk analyses. Graphitic carbon inside apatite is associated with nanometre-size ammoniated phyllosilicate. Precursors of these metamorphic minerals and graphitic carbon originated from ferruginous clay-rich sediments with biomass. We conclude that graphite coatings and inclusions in apatite grains indicate fluid remobilization during amphibolite-facies metamorphism of precursor biomass. This new evidence fills in observational gaps of metamorphosed biomass into graphite and supports the existence of biosignatures in the highly metamorphosed iron formation from the Eoarchean Akilia Association, which dates from the beginning of the sedimentary rock record.

Supplementary material: Figures illustrating the petrography and analytical results are available at: https://doi.org/10.6084/m9.figshare.c.4430609

Received 14 May 2018; **revised** 1 March 2019; **accepted** 1 March 2019

Understanding the impact of metamorphism on biological organic matter (OM) is a fundamental problem to resolve to determine the origin of carbon in the oldest graphite on Earth and in rocks from other ancient planetary surfaces. The metamorphic alteration of OM is known to lead to the loss of heteroatoms and molecular functional groups (Vandenbroucke & Largeau 2007), as well as to enrichments in heavy carbon and nitrogen isotopes (Boyd 2001*a*; Desmarais 2001). The composition of OM associated with fossils in the rock record can be altered first through diagenesis, when biomass is oxidized by microbes and when sediments are altered by non-equilibrium reactions, dehydration and eventually by metamorphism. The last has the greatest effect on the resulting composition and crystallinity because it leads to the graphitization of carbon, in which heteroatoms and light isotopes are lost from biological OM (Bernard & Papineau 2014). Organic microfossils in Proterozoic rocks metamorphosed at <300°C preserve pristine carbon isotope compositions (House *et al.* 2000; Lepot *et al.* 2013; Williford *et al.* 2013, 2015). In fact, carbon isotope compositions are relatively unaffected by metamorphism at conditions less than the greenschist facies (*P c.* 3–6 kbar and *T c.* 250–450°C), with isotopic fractionations (expressed as $\delta^{13}C = \left(\frac{(^{13}C/^{12}C)_{sample}}{(^{13}C/^{12}C)_{PDB}} - 1\right) \times 1000‰$) only about 2–4‰ from precursor OM (Desmarais 2001). Heteroatoms in OM such as H, N, O and S can also be preserved in OM from microfossils in sedimentary rocks metamorphosed at the greenschist facies (Oehler *et al.* 2009, 2010) and if they can be quantified heteroatom concentrations can serve to distinguish types of kerogen (Vandenbroucke & Largeau 2007). Under high pressure and temperature below 400°C, organic microfossil structures can still be well preserved and can contain carboxylic, alcoholic, phenolic, ketonic and olefinic functional groups (Bernard *et al.* 2007). Some molecular functional groups may also be preserved through metamorphism up to the amphibolite facies (*P c.* 4–9 kbar and *T c.* 450–700°C); however, alkanes tend to be shorter and less abundant owing to thermal cracking (Schwab *et al.* 2005). It is unknown, however, if sedimentary rocks metamorphosed at the high-pressure and high-temperature conditions of the amphibolite facies can preserve graphitic carbons with clear biosignatures that indicate a carbon source from biomass. In other words, it is unclear whether combined mineral, molecular, elemental and isotope signatures can be preserved through such metamorphic regimes

and retain diagnostic characteristics of original biomass. This is important, however, because documentation of biological signatures in graphitic carbon from highly metamorphosed rocks serves as a basis to interpret the geobiological record of the oldest sedimentary rocks and to search for biosignatures in extraterrestrial environments.

Because animal fossils have never been debated as non-biological in origin and are generally preserved as carbonate–apatite mixtures with OM, clays and/or pyrite (Olempska & Wacey 2016), such mineral assemblages in metamorphosed sedimentary rocks can be indicative of mineralized decayed biomass. Sedimentary rocks from late Paleoproterozoic age in the Lake Superior area preserve distinct diagenetic structures such as rosettes and granules (LaBerge 1973; Carrigan & Cameron 1991; Heaney & Veblen 1991; Winter & Knauth 1992; Papineau *et al.* 2017), microfossils (Barghoorn & Tyler 1965; Lougheed 1983; Wacey *et al.* 2013; Shapiro & Konhauser 2015) and stromatolites, which demonstrate that microbial ecosystems were widespread in the studied environment. The samples in the current study came from the *c.* 1.85 Ga Bijiki member of the Michigamme Formation in the Baraga Group, Michigan, USA, and were metamorphosed at the amphibolite facies. The aim of this study is to provide a comprehensive sub-micron-scale documentation of the composition and petrography of graphitic carbon to constrain the preservation of biological OM under amphibolite-facies metamorphic conditions.

The composition of carbon in the amphibolite-facies Michigamme banded iron formation (BIF) is also of particular relevance to the controversial origin of carbon in graphite from the 3.83 Ga Akilia quartz–pyroxene (Akilia Qp) rock, which has been debated as evidence for the earliest life on Earth (Mojzsis *et al.* 1996; Nutman & Friend 2006; McKeegan *et al.* 2007; Papineau *et al.* 2010*a*, *b*), and fluid-deposited graphite of possible non-biological origin (Lepland *et al.* 2002, 2010; Papineau *et al.* 2010*a*). The Akilia Qp rock is an Fe-silicate BIF metamorphosed at the granulite facies at 3.65 Ga ($T > 650$°C and $P > 5$ kbar), retrograded at the amphibolite facies at 2.7 Ga (Manning *et al.* 2006), and finally around the upper greenschist facies at around 1.5 Ga. As in the Michigamme samples in this study, coarse quartz crystals in the Akilia Qp rock are associated with fields of fluid inclusions that commonly contain apatite grains between about 10 and 60 μm, which frequently have graphite coatings (Papineau *et al.* 2010*a*). These sizes of apatite crystals are also consistent with analogous apatite occurrences in metapelites from the granulite-facies metamorphism in the Lachlan Fold Belt in Australia (Nutman 2007). The Bijiki graphite is ^{13}C-depleted and contains trace amounts of biologically important heteroatoms (Papineau *et al.* 2010*b*). However, in rocks from such metamorphic grades, graphite can also be associated with calcite, magnetite and multiphase sulphides, and typically enveloped in amphibole, which complicates interpretations of graphite–apatite associations (Papineau *et al.* 2010*a*). Thus, the possible biological origin of graphite in the Akilia Qp rock remains unclear and debated. Here we make progress on this problem and report new results from the petrologically similar and younger Bijiki BIF that shed some light on the possible biological origin of carbon in graphite from the Akilia Qp rock.

Geology and samples

The Michigamme BIF is just one of several BIF units deposited between 1.85 and 1.83 Ga in the Lake Superior region of North America as a result of hydrothermal and geotectonic activity (Schulz & Cannon 2007). During the accretion of supercontinent Nuna (Laurentia) in the SW Superior Craton, the Penokean Orogeny resulted in the closure of the Baraga Basin in the Marquette range. These events resulted in the closing of many coeval basins with hydrothermal activity that delivered vast quantities of Fe on the seafloor, now preserved as BIF of the Cuyuna, Mesabi, Iron River, Marquette, Gogebic and Gunflint ranges. The Penokean Orogeny is thought to have ended by 1.84 Ga (Schneider *et al.* 2002) and to have resulted in the suture of island arcs and the Wisconsin Magmatic Terrane south of the Superior Craton (Van Wyck & Johnson 1997). Regional volcanism at 1.88 Ga (Rasmussen *et al.* 2012) was swiftly followed by widespread hydrothermal activity and the deposition of late Paleoproterozoic BIF. Notably, if the Lake Superior BIF are stitched back together, the time-correlative Cuyuna and Mesabi ranges in Minnesota, the Iron River, Gogebic and Marquette ranges in Michigan, and the Gunflint range of west Ontario would form a continuous, mostly linear belt more than 600 km long of late Paleoproterozoic BIF–pelite–chert successions (Schulz & Cannon 2007). Collectively, the BIF of the Animikie and Baraga Groups includes various types of mineralogies, including stromatolitic and granular jasper, siderite BIF, grey–red silicate BIF and grey magnetite cherty BIF, and have collectively been metamorphosed at low to high grades, up to the amphibolite and granulite facies in areas of contact metamorphism (French 1964). Age constraints for the Baraga Group are between 1.874 and 1.833 Ga (Fralick *et al.* 2002; Schneider *et al.* 2002; Rasmussen *et al.* 2012). The location of the TVA-294 drill hole is in the area of the Great Lakes tectonic zone in Marquette County in the Upper Peninsula of Michigan, where pre-Penokean rocks have been metamorphosed up to the amphibolite facies during the Penokean Orogeny (Holm *et al.* 2007).

Drill core TVA-294 was drilled by the Ford Motor Company into the Dead River Basin in the Upper Peninsula of Michigan and the studied samples come from a section of this core located between 190 and 200 m depth (621–659 feet) (Fig. 1a). The Michigamme Fe-silicate BIF (because of their varied mineralogy and metamorphic grade, Fe-silicate BIF have also been variably called by other workers 'banded silicate formation', 'silicate-facies BIF', 'quartz–pyroxene rock' and 'slaty taconite' in the literature) contains graphite-rich layers (Fig. 1b) as well as pyroxene, grunerite and magnetite bands with subordinate quartz, biotite, stilpnomelane,

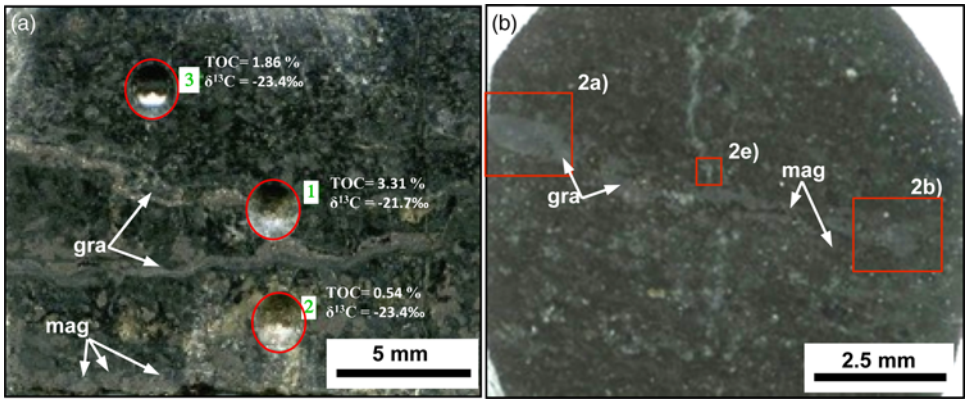

Fig. 1. Petrography of graphite in the Michigamme silicate BIF. (**a**) Reflected light image of graphite layers in polished slab where the C-isotope compositions were measured on micro-drilled powders (red circles); (**b**) reflected light image of the round polished slab used for SIMS spot analyses (red boxes 2a and 2b) and FIB-based nanofabrication (box 2e). Mineral abbreviations: gra, graphite; mag, magnetite.

anthophyllite, chlorite, carbonate, apatite, graphite, pyrite and pyrrhotite (Fig. 2; Table 1). Associated sedimentary rocks from this drill core contain garnet and inosilicate minerals that confirm metamorphism at the amphibolite facies. Dolomitic carbonate veins in this rock cross-cut layers and contain apatite grains between 5 and 50 μm in size associated with inclusions and coatings of graphitic carbon (Papineau *et al*. 2010*b*). In the same rock, apatite grains are concentrated in layers and, based on trace elements of co-occurring graphite, they have been argued to have been sourced from biomass (Papineau *et al*. 2010*b*).

Here we consider the potential contamination by more recent biological activity and fluids. Because Holocene glacial till is preserved as scattered pockets of soils around the Upper Peninsula of Michigan, soils are thin and sparse, and the underlying bedrocks are Late Paleoproterozoic metasediments. Whereas samples from outcrops are more susceptible to contamination by modern growth (e.g. from lichens and fungus), the studied samples were all from a drill core of Fe ore for the benefit of prospectors for the Ford Motor Company, well separated from the reach of these modern organisms. Although phylogenetic analyses suggest that modern microorganisms can colonize and contaminate drill core material (Gérard *et al*. 2009), these microorganisms are probably only in trace abundance and the timing of their colonization of drill cores remains unknown. Considering the paucity of other sources of biomass younger than the Late Paleoproterozoic depositional age, we do not expect that young organic molecules could be contaminants in the drill core specimens that we studied. However, contamination by drilling fluids and by late, but not modern, infiltration of OM remains possible and needs to be evaluated in light of the expected crystallinity of graphitic carbons in metamorphosed rocks.

Analytical methods

Micro-Raman spectroscopy

Raman spectroscopy was performed on a separate polished slab, about 1 cm diameter by about 0.5 cm in thickness, using a WITec α300 Confocal Raman imaging system at the University College London (UCL). A 532 nm laser was used and focused at 1000× magnification for a single acquisition of 100 integrations of 1 s spectra. An optical fibre of 50 μm in diameter was used to collect a Raman spectrum at a confocal depth of 2 μm below the polished surface of a thin section and inside transparent minerals, which minimizes the chances of spectral acquisition with artificially disordered graphite caused by polishing. The resulting average spectrum was corrected with a background subtraction of a polynomial fit of order four. Raman D1, D2 and G peaks in the spectra were then modelled with Lorentz-fitted curves. The hyperspectral image was created from filters at 965 cm^{-1} (width of 20 cm^{-1}) for apatite, 1090 cm^{-1} (width 20 cm^{-1}) for carbonate, 1575 cm^{-1} (width 60 cm^{-1}) for graphite, and 1347 cm^{-1} (width 20 cm^{-1}) for PCG.

Focused ion beam nanofabrication

Focused ion beam (FIB) milling and lift-out were performed using an FEI Nova 600 dual beam FIB-SEM (scanning electron microscope) at the US Naval Research Laboratory. For FIB nanofabrication, a rock slab was shaped into a disc and was polished with 250 nm Al_2O_3 and deionized (DI) water, rinsed with DI water, rinsed with isopropyl alcohol, dried with a dry N_2 blower and covered with a *c.* 10 Å Au coat. The polished rock slab, which was never in contact with epoxy, was inserted into the FIB-SEM, and a Pt shield was then deposited on the surface of the target prior to milling. A focused 30 keV Ga^+ primary beam was then used to mill away material from both sides of the deposited Pt shield to expose the lamella. Following lift-out and welding onto an Omniprobe transmission electron microscope (TEM) half-grid made of Cu, the lamella was thinned down to *c.* 100 nm with progressively smaller beam currents (Wirth 2009) (down to 20 pA at 30 keV).

Scanning electron microscopy with energy-dispersive spectroscopy and electron probe micro-analysis with wavelength-dispersive spectroscopy

These analyses were performed at the Department of Earth Sciences at UCL using a JEOL JSM-6480L SEM and at the Carnegie Institution of Washington with the JEOL 8900 Superprobe, respectively. In the SEM, the electron beam was set at 0.5 nA and 15 keV, whereas in the electron probe micro-analysis (EPMA) the

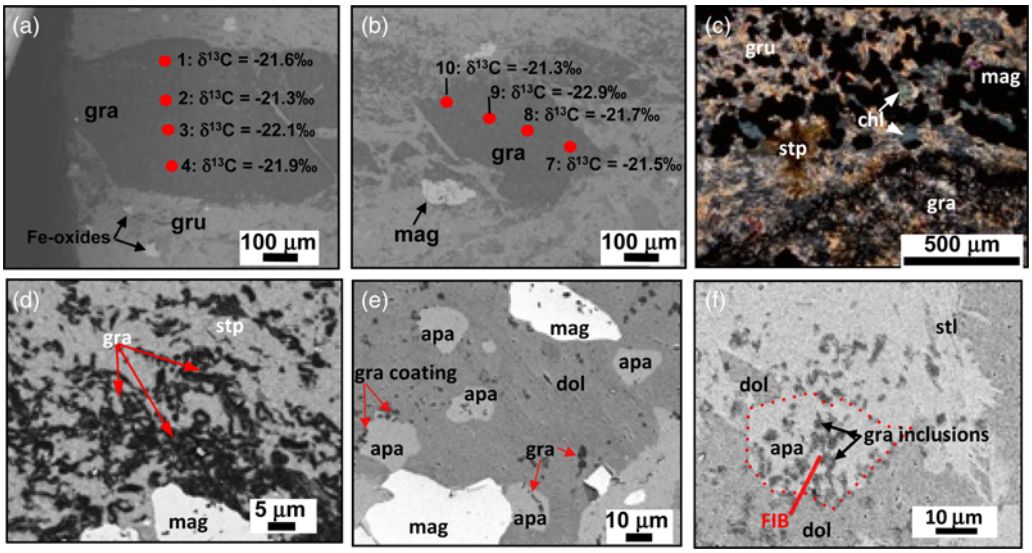

Fig. 2. Petrography of apatite and graphite in the Michigamme silicate BIF. (**a**, **b**) Secondary electron images of spot locations analysed by SIMS showing the corrected $\delta^{13}C$ values in Table 2; (**c**) crossed-polars transmitted light image of the silicate matrix that embeds layers of coarse euhedral magnetite; (**d**) backscattered electron (BSE) image of graphite filaments in silicate matrix; (**e**) BSE image of apatite grains with graphite coatings in dolomite vein; (**f**) BSE image of apatite associated with graphite, dolomite and phyllosilicate, targeted for FIB (lamella location is shown as a red line). Mineral abbreviations: gra, graphite; apa, apatite; dol, dolomite (Mn- and Fe-rich); gru, grunerite; chl, chlorite; stl, stilpnomelane; mag, magnetite.

Table 1. *Elemental compositions of apatites, carbonates and silicates obtained from EDS and WDS analyses*

	Apatites analysed by WDS in the EPMA			
Target:	TVA294-659.6	TVA294-659.6	TVA294-659.6	TVA294-659.6
Element wt%/spot:	3	12	14	4
CaO	55.1	54.5	55.0	55.1
P_2O_5	41.2	41.5	40.6	40.9
F	3.2	3.2	3.3	3.2
Cl	0.0	0.0	0.0	0.0
FeO	0.5	0.6	1.0	0.4
MnO	0.2	0.3	0.2	0.2
Na_2O	0.0	0.0	0.0	0.0
MgO	0.0	0.0	0.0	0.0
SiO_2	0.0	0.0	0.0	0.0
Ce_2O_3	0.1	0.1	0.0	0.1
Y_2O_3	0.0	0.0	0.0	0.0
Total	99.1	98.8	98.8	98.7
	Fluorapatite	Fluorapatite	Fluorapatite	Fluorapatite

	Fe-silicates analysed by EDS in the TEM (on FIB lamellae; spots shown in inset of Fig. 4e)	
Target:	TVA294-656.9	TVA294-656.9
Element wt%/spot:	01b	01a
O K	48.6	49.9
Mg K	0.4	0.4
Al K	0.8	0.5
Si K	36.9	39.6
Ca K	0.7	0.8
Mn K	0.4	0.2
Fe K	12.2	8.6
Total	100.0	100.0
	Ca–Mn-stilpnomelane	Ca–Mn-stilpnomelane

	Ferric–ferrous silicates analysed by EDS in the SEM						
Target:	TVA294-622.1	TVA294-622.1	TVA294-622.1	TVA294-622.1	TVA294-622.1	TVA294-622.1	TVA294-622.1
Element wt%/spot:	1	2	5	8	7	4	6
C K			14.3				13.0
O K	36.2	36.1	36.3	37.1	39.9	39.2	37.8
Mg K	5.9	5.2	4.1	5.6	5.5	5.1	4.0
Al K					11.2	8.9	8.2
Si K	26.9	26.2	19.5	25.6	12.6	13.9	10.1
K K						1.4	
Mn K	2.3	1.8	1.9	2.7			
Fe K	28.8	30.7	24.0	29.1	30.8	31.5	26.9
Total	100.0	100.0	100.0	100.0	100.0	100.0	100.0
	Proto-Mn,Fe-anthophylite	Mn,Fe-anthophylite	Mn,Fe-anthophyllite + graphite	Grunerite	Chlorite	Chlorite	Graphite with chlorite

	Sulphides and oxides with graphitic carbon analysed by EDS in the SEM			
Target:	TVA294-622.1	TVA294-622.1	TVA294-622.1	TVA294-622.1
Element wt%/spot:	1	3	9	2
C K		22.4		8.8
O K			11.5	22.9
S K	34.7	26.7	22.3	
Fe K	65.3	50.9	66.2	68.3
Total	100.0	100.0	100.0	100.0
	Pyrrhotite	Pyrrhotite + graphite	oxidized pyrite	Magnetite + graphite

	Carbonates analysed by EDS in the SEM					
Target:	TVA294-656.9	TVA294-656.9	TVA294-622.1	TVA294-622.1	TVA294-622.1	TVA294-622.1
Element wt%/spot:	1	2	4	5	6	3
C K	15.5	13.6	13.6	13.6	11.7	63.2
O K	43.0	34.4	43.2	43.2	45.1	20.9
Mg K	9.8	9.8	6.1	6.1	6.7	2.2
Cl K					1.4	
Ca K	26.0	24.8	21.4	21.4	20.7	7.9
Si K	1.1	1.1				0.6
Mn K	4.5	4.9	6.5	6.5	5.4	2.5
Fe K		11.0	9.2	9.2	9.2	2.8
Total	99.9	99.6	100.0	100.0	100.0	100.0
	Mn-dolomite	Mn–Fe-dolomite	Mn–Fe-dolomite	Mn–Fe-dolomite	Mn–Fe-dolomite	Graphite in dolomite

beam was 5 nA at 30 keV, for spot sizes around 1 μm. The polished rock slab was C-coated prior to EPMA. Abundances were determined by EPMA using five wavelength-dispersive spectrometers (WDS) and standards of Durango apatite, and in-house sulphide, garnet and other silicates, which yield an error of around 0.1 wt% oxide. Other elemental abundances were measured by scanning electron microscopy with energy-dispersive spectroscopy (SEM-EDS) at UCL on Au-coated samples and were obtained from spectra subtracted of Au, corrected with an XPP matrix correction routine in the Oxford Instruments Inca© software, and normalized to 100.0%, which yields an error around 5%.

Transmission electron microscopy

High- and low-resolution TEM analysis of the lamella was performed with a 200 keV JEOL JEM 2500SE at the Astromaterials Research and Exploration Science e-beam facility at NASA Johnson Space Center (JSC) and with a 200 keV JEOL JEM 2100 in the Department of Chemistry at UCL. The TEM at JSC uses a field emission electron source, whereas the TEM at UCL uses a LaB_6 electron source. Detailed mineralogy of the FIB lamella was characterized in both conventional bright-field imaging mode and in scanning (STEM) mode using both bright-field (BF, unscattered electrons) and dark-field (DF, scattered electrons) detectors. Elemental maps and selected 'spot' compositional analyses were acquired at JSC using a Noran energy-dispersive X-ray spectrometer (EDS) in STEM mode and at UCL using a liquid nitrogen cooled EDS detector.

Synchrotron-based scanning transmission X-ray microscopy

Samples were analysed with the polymer synchrotron-based scanning transmission X-ray microscopy (STXM) beamline 5.3.2.2 at the Advanced Light Source (ALS), Lawrence Berkeley National Laboratory (Kilcoyne *et al*. 2003). During analysis, the electron current in the storage ring was held constant in 'topoff mode' at 500 mA at energy of 1.9 GeV, providing a nearly constant flux of photons at the STXM end-station. The dispersive and non-dispersive exit slits were set at 25 μm. Focusing of the photon beam is produced by a Fresnel zone plate with a spot size of around 30 nm. STXM data were acquired as spectral image stacks (i.e. a series of X-ray absorption images at sequential energies), from which X-ray absorption near-edge structure (XANES) spectra of regions of interest were extracted. The highest spectral resolution (0.1 eV step between subsequent images) was in the 282–292 eV range, where the near-edge spectral features for electronic transitions from core shell states to anti-bonding σ*- and π*-orbitals are located. XANES spectra are presented as the ratio of transmission spectra from the region of interest, I, relative to background transmission spectra, I_0, calculated as $A = -\ln(I/I_o)$. Modelling of the CNO spectrum was performed by fitting the Henke mass absorption coefficient curves for those elements to the entire XANES spectrum (Alléon *et al*. 2015).

Secondary ion mass spectrometry and nanoSIMS

Secondary ion mass spectrometry (SIMS) analyses were performed on the gold-coated polished slab, after FIB but before EPMA analyses, and were to measure the $\delta^{13}C$ value of graphite with a Cameca ims 6F ion probe at the Carnegie Institution of Washington. Analytical conditions include extreme energy filtering conditions (350 eV offset from −5 keV) and the use of the first field aperture and second energy slit. Each analysis consisted of 15 blocks of 10 cycles with a 3σ data rejection of cycles for an analysis time of 25 min, including 3 min of pre-sputtering. The primary Cs^+ beam current was continuously monitored and kept at 3.0 ± 0.2 nA, to ensure at least 5×10^8 counts for the ^{12}C signal, which yielded an internal error better than 0.05%. Spot size was set at 30 μm. The external error was calculated for a bracketing series of spot analyses on an in-house graphite (BH-graphite from Sri Lanka; Farquhar *et al*. 1999; $n = 34$) and diamond (standard N198; $n = 15$) (Table 2). Reproducibility was calculated as the square root of the sum of the internal error square plus the external error square, and averages ±2.0‰ (2σ).

Nanoscale secondary ion mass spectrometry (nanoSIMS) analyses were performed on the FIB lamella prior to final thinning by Ne. The TEM half-grid with the FIB lamella was mounted on a clean polished Al stub using colloidal silver paint before insertion in the nanoSIMS holder, following the STXM analyses. Analyses were performed as before (Papineau *et al*. 2010*b*), but an electron gun was used for charge compensation owing to loss of electrons in addition to extracted negative secondary ions, because the FIB lamella is essentially an uncoated insulator. Although a graphite standard was unavailable during these analyses, atomic ratios of C/N and C/O were calibrated using quantitative atomic ratios estimated from STXM measurements on the same areas in the FIB lamella, using the method described by Alléon *et al*. (2015), and here tentatively applied to also include O/C estimates. We note that there are a number of possible model curves, and we chose the one that best showed the overall trend of the selected line spectrum. Unfortunately, the nanoSIMS map for O/C was deemed to unreliably show this atomic ratio in graphite owing to signal contamination by the phyllosilicate, apatite and dolomite surrounding the graphitic carbon, a spatial limitation of the technique, which did not allow quantification of the O/C atomic ratio from the CNO-XANES spectrum.

Helium–neon focused ion beam milling and microscopy

Surface analyses of the FIB lamella by He–Ne microscopy were performed using a Zeiss Orion NanoFAB FIB instrument located at the London Centre for Nanotechnology at UCL. Final thinning of the lamella was performed with a 1.6–0.8 pA focused beam of Ne^+ and secondary electron images were acquired using a 0.4 pA focused beam of He^+. The He^+ and Ne^+ ions were accelerated to 25 keV and 15 keV respectively. Although the decreased Ne acceleration voltage typically results in a larger probe size it has previously been shown that lower landing energies for ion result in increased fidelity of milling (Tan *et al*. 2010). Organic contamination of the surface of the FIB lamella was minimized by cleaning the Orion NanoFab sample chamber using an oxygen plasma generated by an Evactron® system.

Atomic force microscopy

Atomic force microscopy (AFM) was then used to measure the surface topography and evaluate the roughness of the lamella using a Dimension 3100 system at the London Centre for Nanotechnology at UCL with the following analytical configuration parameters: tapping mode AFM (TM-AFM) was carried out on the Dimension 3100 with a Nanoscope IV controller (Bruker Ltd., UK) equipped with a closed loop scanner. PPP-NCH cantilevers (Nanosensors™) with an average spring constant of 42 N m^{-1} and a nominal tip radius of curvature <10 nm were used for ambient air TM-AFM. The cantilevers were oscillated near their resonant frequency with a free amplitude at resonance of 2 V. The amplitude setpoint was set to 80% of the value of the free amplitude. Typical scan rate was 1 Hz.

Auger electron spectroscopy

The local Auger electron spectroscopy (AES) measurements were performed at room temperature in a UHV chamber (instrument base pressure $<2 \times 10^{-10}$ mbar) equipped with a Leo Gemini

Table 2. *In situ carbon isotope analyses by SIMS on graphite band from TVA294-659.6 and standards**

Analysis no.	Analysis spot name	$^{13}C/^{12}C$ (uncorr.)	Error	^{12}C count rate (counts s^{-1})	^{12}C counts	I primary (nA)	$^{13}C/^{12}C$ (IMF corr.)	$\delta^{13}C$ (‰)	Internal error (1σ)	External error (2σ)
1	N198a@2	1.04659E − 02	4.12E − 06	8.67E + 05	1.30E + 08	3.27	1.11208E − 02	−9.2	0.4	2.0
2	N198a@3	1.04666E − 02	4.53E − 06	8.72E + 05	1.31E + 08	3.25	1.11215E − 02	−9.2	0.4	2.0
3	N198a@4	1.04786E − 02	4.18E − 06	8.68E + 05	1.30E + 08	3.21	1.11343E − 02	−8.0	0.4	2.0
4	N198a@5	1.04638E − 02	4.08E − 06	8.69E + 05	1.30E + 08	3.18	1.11186E − 02	−9.4	0.4	2.0
5	N198a@6	1.04796E − 02	3.87E − 06	8.64E + 05	1.30E + 08	3.16	1.11354E − 02	−8.0	0.4	2.0
6	N198a@7	1.04731E − 02	4.14E − 06	8.22E + 05	1.23E + 08	3.08	1.11284E − 02	−8.6	0.4	2.0
7	N198a@8	1.04715E − 02	3.39E − 06	8.49E + 05	1.27E + 08	3.12	1.11267E − 02	−8.7	0.3	2.0
8	N198a@9	1.04735E − 02	4.04E − 06	8.56E + 05	1.28E + 08	3.14	1.11289E − 02	−8.5	0.4	2.0
9	N198a@10	1.04856E − 02	3.97E − 06	8.62E + 05	1.29E + 08	3.09	1.11417E − 02	−7.4	0.4	2.0
10	N198a@11	1.04895E − 02	4.34E − 06	8.65E + 05	1.30E + 08	3.12	1.11459E − 02	−7.0	0.4	2.0
11	N198a@12	1.04829E − 02	4.40E − 06	8.57E + 05	1.29E + 08	3.11	1.11389E − 02	−7.6	0.4	2.0
12	N198a@13	1.04928E − 02	4.27E − 06	8.56E + 05	1.28E + 08	3.06	1.11494E − 02	−6.7	0.4	2.0
13	N198a@14	1.04770E − 02	4.50E − 06	8.43E + 05	1.26E + 08	3.08	1.11326E − 02	−8.2	0.4	2.0
14	N198a@15	1.04857E − 02	4.09E − 06	8.44E + 05	1.27E + 08	3.09	1.11418E − 02	−7.4	0.4	2.0
15	N198a@16	1.04869E − 02	4.44E − 06	8.50E + 05	1.27E + 08	3.05	1.11431E − 02	−7.3	0.4	2.0
16	BH_graphite@1	1.04838E − 02	4.73E − 06	7.24E + 05	1.09E + 08	3.04	1.11398E − 02	−7.6	0.5	2.1
17	BH_graphite@2	1.04950E − 02	4.54E − 06	7.05E + 05	1.06E + 08	3.02	1.11517E − 02	−6.5	0.4	2.0
18	BH_graphite@3	1.04853E − 02	4.11E − 06	7.20E + 05	1.08E + 08	2.99	1.11414E − 02	−7.4	0.4	2.0
21	BH_graphite@6	1.04610E − 02	4.90E − 06	6.03E + 05	9.04E + 07	3.11	1.11156E − 02	−9.7	0.5	2.1
22	BH_graphite@7	1.04700E − 02	5.30E − 06	6.16E + 05	9.23E + 07	3.07	1.11252E − 02	−8.9	0.5	2.1
23	BH_graphite@8	1.04810E − 02	4.66E − 06	6.06E + 05	9.09E + 07	3.03	1.11368E − 02	−7.8	0.4	2.1
24	BH_graphite@9	1.04799E − 02	4.79E − 06	6.23E + 05	9.35E + 07	2.84	1.11357E − 02	−7.9	0.5	2.1
25	BH_graphite@10	1.04781E − 02	4.72E − 06	6.21E + 05	9.32E + 07	2.76	1.11338E − 02	−8.1	0.5	2.1
26	BH_graphite@11	1.04712E − 02	4.40E − 06	6.21E + 05	9.31E + 07	2.92	1.11264E − 02	−8.7	0.4	2.0
34	BH_graphite@12	1.04775E − 02	4.88E − 06	5.89E + 05	8.84E + 07	3.30	1.11331E − 02	−8.1	0.5	2.1
35	BH_graphite@13	1.04899E − 02	4.83E − 06	5.74E + 05	8.60E + 07	3.28	1.11463E − 02	−7.0	0.5	2.1
36	BH_graphite@14	1.04869E − 02	4.91E − 06	5.61E + 05	8.41E + 07	3.27	1.11431E − 02	−7.3	0.5	2.1
37	BH_graphite@15	1.04739E − 02	5.13E − 06	5.16E + 05	7.73E + 07	3.04	1.11293E − 02	−8.5	0.5	2.1
38	BH_graphite@16	1.04632E − 02	5.79E − 06	5.39E + 05	8.09E + 07	3.04	1.11179E − 02	−9.5	0.6	2.2
39	BH_graphite@17	1.04860E − 02	5.27E − 06	5.12E + 05	7.68E + 07	3.03	1.11422E − 02	−7.3	0.5	2.1
46	BH_graphite@18	1.04743E − 02	5.12E − 06	5.24E + 05	7.86E + 07	2.96	1.11297E − 02	−8.5	0.5	2.1
47	BH_graphite@19	1.04901E − 02	5.30E − 06	5.04E + 05	7.56E + 07	2.94	1.11465E − 02	−7.0	0.5	2.1
48	BH_graphite@20	1.04813E − 02	5.32E − 06	5.09E + 05	7.63E + 07	2.90	1.11372E − 02	−7.8	0.5	2.1
54	BH_graphite2@1	1.04712E − 02	4.83E − 06	6.97E + 05	1.05E + 08	3.49	1.11264E − 02	−8.7	0.5	2.1
55	BH_graphite2@2	1.04774E − 02	4.45E − 06	7.17E + 05	1.08E + 08	3.47	1.11330E − 02	−8.2	0.4	2.0
56	BH_graphite2@3	1.04744E − 02	4.59E − 06	7.31E + 05	1.10E + 08	3.44	1.11298E − 02	−8.4	0.4	2.0
67	BH_graphite2@4	1.04792E − 02	4.71E − 06	7.28E + 05	1.09E + 08	3.30	1.11349E − 02	−8.0	0.4	2.1
68	BH_graphite2@5	1.04674E − 02	4.59E − 06	7.35E + 05	1.10E + 08	3.27	1.11224E − 02	−9.1	0.4	2.1
69	BH_graphite2@6	1.04747E − 02	4.38E − 06	7.43E + 05	1.11E + 08	3.26	1.11301E − 02	−8.4	0.4	2.0
70	BH_graphite2@7	1.04716E − 02	4.10E − 06	7.46E + 05	1.12E + 08	3.23	1.11269E − 02	−8.7	0.4	2.0
71	BH_graphite2@8	1.04647E − 02	4.49E − 06	7.33E + 05	1.10E + 08	3.22	1.11195E − 02	−9.4	0.4	2.0
72	BH_graphite2@9	1.04865E − 02	4.72E − 06	7.12E + 05	1.07E + 08	3.20	1.11427E − 02	−7.3	0.4	2.1
73	BH_graphite2@10	1.04899E − 02	4.55E − 06	7.10E + 05	1.07E + 08	3.22	1.11463E − 02	−7.0	0.4	2.0
74	BH_graphite2@11	1.04971E − 02	4.76E − 06	6.75E + 05	1.01E + 08	3.21	1.11539E − 02	−6.3	0.5	2.1
79	BH_graphite2@13	1.04540E − 02	4.95E − 06	5.81E + 05	8.71E + 07	3.07	1.11081E − 02	−10.4	0.5	2.1
80	BH_graphite2@14	1.04561E − 02	5.28E − 06	5.81E + 05	8.72E + 07	3.09	1.11104E − 02	−10.2	0.5	2.1
88	BH_graphite2@17	1.04880E − 02	5.05E − 06	5.36E + 05	8.04E + 07	3.08	1.11443E − 02	−7.2	0.5	2.1
106	BH_graphite2@20	1.04763E − 02	4.67E − 06	5.49E + 05	8.23E + 07	2.83	1.11318E − 02	−8.3	0.4	2.1
107	BH_graphite2@21	1.04660E − 02	4.66E − 06	5.65E + 05	8.48E + 07	2.88	1.11209E − 02	−9.2	0.4	2.1
108	BH_graphite2@22	1.04711E − 02	5.01E − 06	5.63E + 05	8.44E + 07	2.82	1.11263E − 02	−8.8	0.5	2.1
57	TVA294-6596@1	1.03354E − 02	5.36E − 06	5.73E + 05	8.60E + 07	3.43	1.09821E − 02	−21.6	0.5	2.1
58	TVA294-6596@2	1.03385E − 02	5.03E − 06	5.89E + 05	8.83E + 07	3.39	1.09854E − 02	−21.3	0.5	2.1
59	TVA294-6596@3	1.03297E − 02	4.93E − 06	5.78E + 05	8.68E + 07	3.41	1.09761E − 02	−22.1	0.5	2.1
60	TVA294-6596@4	1.03323E − 02	5.47E − 06	5.71E + 05	8.57E + 07	3.38	1.09788E − 02	−21.9	0.5	2.1
61	TVA294-6596@5	1.03359E − 02	4.95E − 06	5.98E + 05	8.97E + 07	3.33	1.09827E − 02	−21.6	0.5	2.1
62	TVA294-6596@6	1.03383E − 02	4.56E − 06	5.92E + 05	8.88E + 07	3.34	1.09852E − 02	−21.3	0.4	2.1
63	TVA294-6596@7	1.03362E − 02	5.73E − 06	5.56E + 05	8.34E + 07	3.31	1.09830E − 02	−21.5	0.6	2.2
64	TVA294-6596@8	1.03347E − 02	6.08E − 06	5.29E + 05	7.94E + 07	3.34	1.09814E − 02	−21.7	0.6	2.2
65	TVA294-6596@9	1.03220E − 02	5.34E − 06	5.31E + 05	7.96E + 07	3.33	1.09679E − 02	−22.9	0.5	2.1
66	TVA294-6596@10	1.03383E − 02	5.38E − 06	4.94E + 05	7.41E + 07	3.32	1.09852E − 02	−21.3	0.5	2.1

*The two in-house standards used were diamond N198 ($\delta^{13}C = -6.0$‰, IMF correction factor is −60.8‰) and BH-graphite ($\delta^{13}C = -8.2$‰, IMF correction factor is −58.9‰).

electron column (resolution <3 nm) at the Friedrich-Alexander-Universität Erlangen–Nürnberg, Germany. The electron beam of the SEM was used as ionization source, with a beam energy of 15 keV and a nominal probe current of 3 nA. Spectra were recorded with a hemispherical electron energy analyser (EA125, Omicron Nanotechnology) and Matrix 3.1 electronics and software (Omicron Nanotechnology). Data processing was performed with Igor Pro 6.22A (Wavemetrics). The depicted spectra were normalized such that both spectra have the same intensity at $E_{Kin} = 950$ eV (i.e. the background level). The quantitative atomic per cent values given were estimated based on the relevant peak areas (after linear background subtraction) and the corresponding element-specific sensitivity factors of 1.07, 0.38 and 0.35 for C, N and O respectively as theoretically calculated (Mroczkowski & Lichtman 1985). We note that some re-deposition of milled material onto the FIB lamellae, even after careful Ne thinning, could be included in the spectra; hence we choose to include these results regardless of their validity, as they suggest new analytical possibilities.

Isotope ratio mass spectrometry

Powder from drillates were obtained using a dental drill bur of SiC and 2 mm in diameter and about 2 mm deep, after discarding the first powder generated, which yields about 1–5 mg of rock powder. Samples accurately weighed to microgram precision were decarbonated in Ag boats, pre-muffled at 600°C for 2 h, using 60–100 µl of sequanal grade 10% HCl (Pierce©). The decarbonated powders were then dried in a laminar airflow hood for more than 4 days. The samples were then combusted using a Carlo Erba elemental analyser coupled to a Delta XL isotope ratio mass spectrometry (IRMS) system linked with a Conflo III gas injection system at the Carnegie Institution of Washington. Standards of Peru Mud and acetanilide were used to determine the accuracy and, combined with the precision (around 0.05‰), yield an error better than 0.3‰ consistent with long-term reproducibility of $\delta^{13}C$ values on these phases.

Results

Petrology of graphite and apatite in an amphibolite-facies silicate BIF

In thin section, the amphibolite-facies Michigamme silicate BIF contains ferrous silicate bands interlayered with magnetite, quartz and carbonate-rich layers, which can also be rich in OM (Fig. 2a–c; supplementary material Fig. S1a and b). Occurrences of ferric–ferrous silicates include manganese-bearing proto-ferro-anthophyllite, grunerite, garnet, biotite, stilpnomelane and green–brown chlorite (Table 1 and Fig. 2c, Fig. S1a–c). Graphitic carbon in these rocks occurs as massive layers free of clays or sulphides up to about 1 mm in thickness (Fig. 1b), and also as wavy, curvy and circular filamentous structures in the silicate matrix (Fig. 2d, Fig. S2b and c) (Papineau *et al.* 2010*b*), as coatings and inclusions in about 78% of apatite grains that form in layers parallel to bedding (Papineau *et al.* 2010*b*), and as disseminated filamentous fragments in Mn–Fe-dolomite veins and layers (Fig. 2e and f, Fig. S2e and f). Magnetite grains are less than 1 mm in size (Fig. 1) and sometimes contain sulphides as micron-size spheroidal inclusions (Fig. S1c). Collectively, the mineral assemblage is consistent with recrystallization under amphibolite-facies conditions.

Raman spectra of both poorly crystalline graphite and well-ordered graphite associated with apatite from elsewhere in this dolomite vein have G peaks located at 1575 cm^{-1} and D peaks located around 1347 cm^{-1} (Fig. 3), the typical position for graphite and identical to a previous report (Papineau *et al.* 2010*b*). The spectrum of well-ordered graphite was used to calculate a maximum

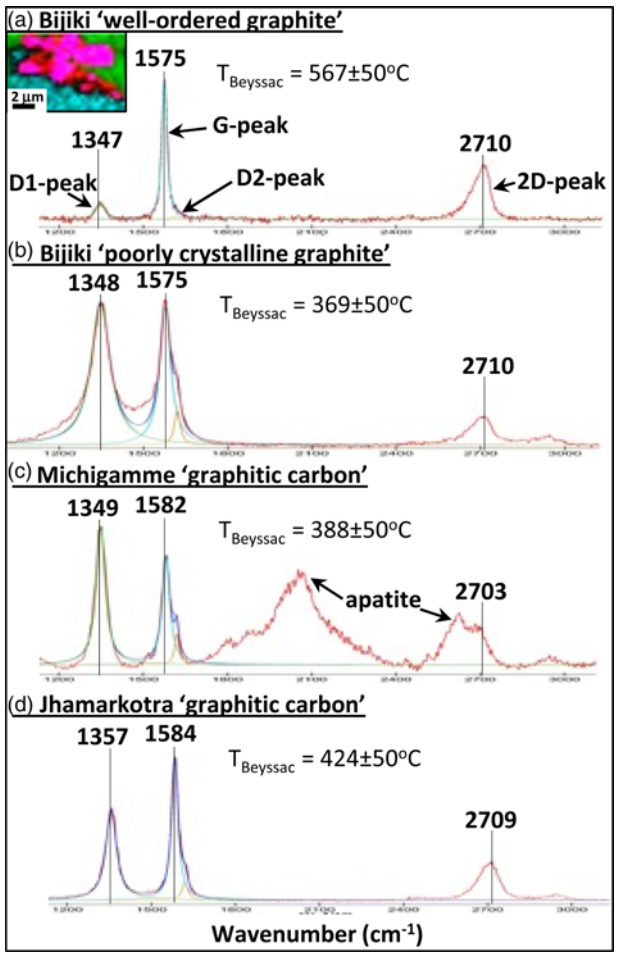

Fig. 3. Raman spectra of mixed graphitic carbons in the immediate vicinity of the nano-fabricated FIB lamella in Bijiki sample TVA294-659.6 (**a**, **b**) compared with other late Paleoproterozoic graphitic carbons (**c**, **d**). The inset is a hyperspectral Raman image of Bijiki graphitic carbons showing 'well-ordered graphite' in red (spectrum shown in (**a**)), mixed with PCG in purple (spectrum shown in (**b**)), and apatite and carbonate in turquoise and green, respectively. Similar spectra of graphitic carbons from contemporary phosphatic rocks metamorphosed at the greenschist to upper greenschist facies are shown for comparison in (**c**) for the Michigamme Formation (sample MA0708, Papineau *et al.* 2017) and in (**d**) for the Jhamarkotra Formation (sample UV0807, Papineau *et al.* 2016). The measured spectra of these graphitic carbons (red) were modelled using a linear combination of Lorentz-fitted peaks (blue) for each of the D1 (green), D2 (orange) and G (turquoise) peaks. Peak metamorphic temperatures were all estimated from the Raman geothermometer of Beyssac *et al.* (2002*a*), calibrated with minerals in metapelite.

metamorphic crystallization temperature (Beyssac *et al.* 2002*a*) of 567 ± 50°C, consistent with amphibolite-facies metamorphism, and matches graphite with a slightly expanded lattice structure from similar mineral assemblages, previously published from this rock (Papineau *et al.* 2010*b*). Some Raman spectra display a more intense and broad D1 peak than graphitic carbon, but it is unclear whether this is due to polishing artefact (Pasteris 1989), variable structures of turbostratic carbon (Beyssac *et al.* 2002*b*), variably crystallized graphitic carbon (Dodd *et al.* 2019), or possibly also a younger, remobilized, more disordered kind of organic matter. The Raman spectrum shows that this disordered graphitic carbon, or poorly crystalline graphite (PCG from hereon), has the same peak positions for its D1, D2, G and 2D peaks as the well-ordered graphite (Fig. 3a and b). High-resolution Raman imaging shows that the two are finely mixed (inset in Fig. 3a). The calculated crystallization temperature for the PCG was calculated to be 369°C, which may not

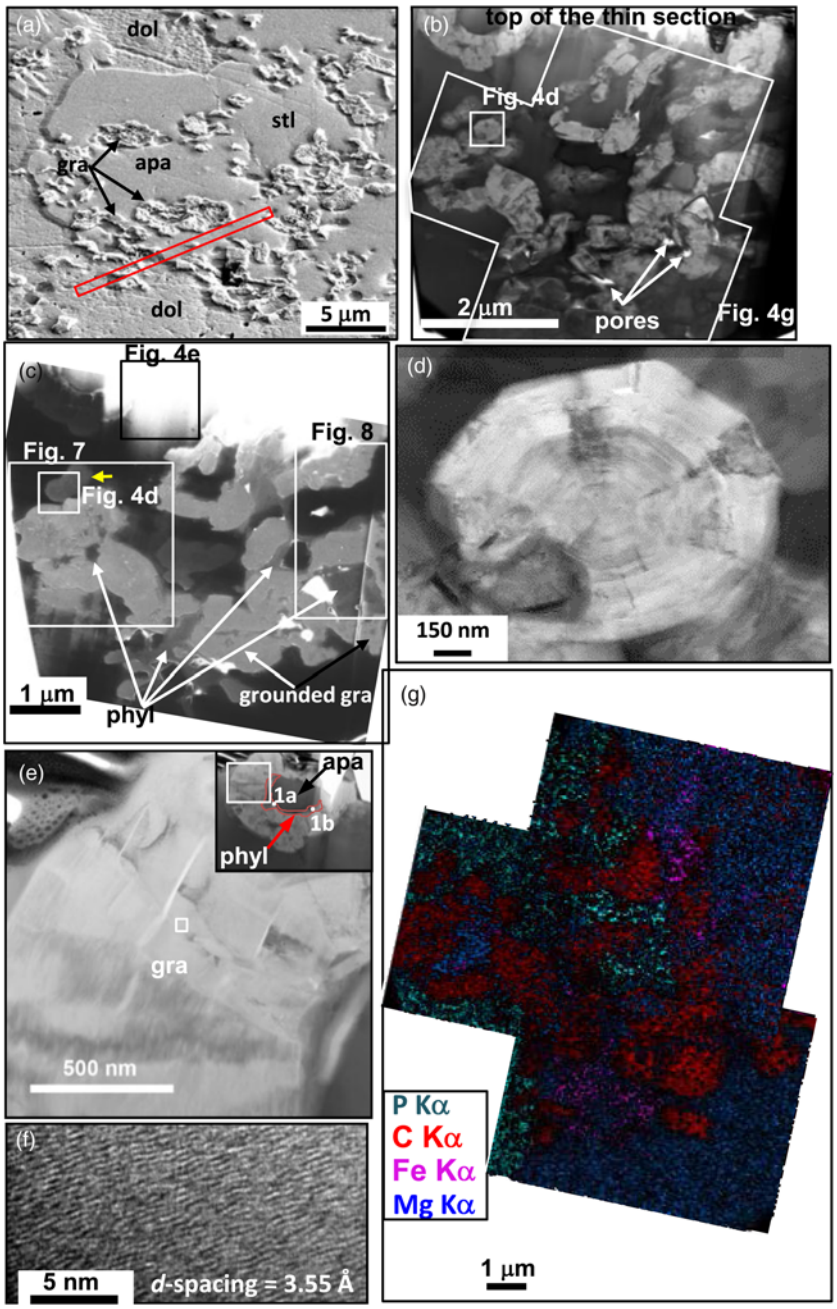

Fig. 4. Apatite grain with graphite filaments from TVA294-659.6. (**a**) Secondary electron image of the targeted apatite grain; (**b**) bright-field TEM image of graphite (light grey) in the apatite + dolomite matrix (dark grey) prior to Ne thinning; white spots are pores in the rock; (**c**) He secondary electron image, which best highlights the thin phyllosilicate (medium grey) coatings on graphite (light grey) inside apatite and dolomite (dark grey); (**d**) cross-section view of concentrically zoned and well-ordered graphite spherulite; (**e**) longitudinal section of a well-ordered graphite filament associated with phyllosilicate (red area in inset) around an apatite core; (**f**) HRTEM images showing lattice fringes for well-ordered graphite; (**g**) EDS map of four major elements showing the close association of phyllosilicate (purple + blue) with graphite (red) with a legend for colours. Abbreviations: phyl, phyllosilicate; gra, graphite; dol, dolomite; apa, apatite; stl, stilpnomelane.

be accurately estimated, as the Raman thermometer used is based on young organic matter in metapelites (Beyssac *et al.* 2002*a*). The PCG is also similar in its Raman spectrum to graphitic carbons found in similarly aged greenschist- to upper greenschist-facies rocks rich in phosphate elsewhere in the Michigamme Formation and in the Jhamarkotra Formation (Fig. 3c and d).

An apatite grain with graphitic carbon that intersects dolomite from the embedding matrix was targeted for nanofabrication into a lamella with an FIB-SEM (Fig. 2f, Fig. S1d–f) and subsequently thinned with a Ne beam (Fig. S1g–i). Secondary electron images from He ion microscopy, following *in situ* thinning by Ne, show contrast (Fig. 4c) given by the electrical conductivity of the different phases; graphitic carbon appears light grey, except when surrounded by an electrically insulating phase, such as dolomite or apatite. Bright-field TEM images show sub-micron size concentrically-layered flakes of graphite (Fig. 4d) as well as nanoscopic graphite 'books' (Fig. 4e). Both of these types of graphitic carbons occur with phyllosilicate (Fig. 4e, Fig. S2c). Concentric graphite books have a euhedral habit and intimately co-occur with PCG with a more irregular and patchy texture (Fig. S2k and l). The full range of measured *d*-spacings reveals expanded graphite lattices between 3.55 and 3.72 Å (Fig. 2f; Fig. S2i and j). The C-XANES spectra of graphite show well-resolved 285.3 and 291.7 eV peaks, and a depressed region between these without strong peaks (Fig. 5c), consistent with highly ordered graphitic carbon. The presence of these peaks is also akin to graphitic carbons associated with apatite from greenschist- to upper greenschist-facies rocks in the Michigamme and Jhamarkotra formations (Fig. 5c and d; Papineau *et al.* 2016, 2017). Hence, both forms of graphitic carbons found by micro-Raman are represented in the FIB lamella, where they are intimately mixed and have a range of *d*-spacings (Fig. 4f).

Graphitic carbon is systematically in direct contact with a clay-size, ferrous, crystalline silicate phase (Fig. 4c) that forms a complex and delicate network in apatite and dolomite (Fig. 4g). This Fe-silicate phase has 2.08 Å lattice fringes (Fig. S2h) and a composition similar to a calcium end-member of stilpnomelane (Table 1, Fig. S2e), a ferric–ferrous phyllosilicate with several crystal orientations showing lattice spacings around 2.1 Å (Gruner 1937; Blake 1965). We note, however, that there is only <1 wt% Al in this

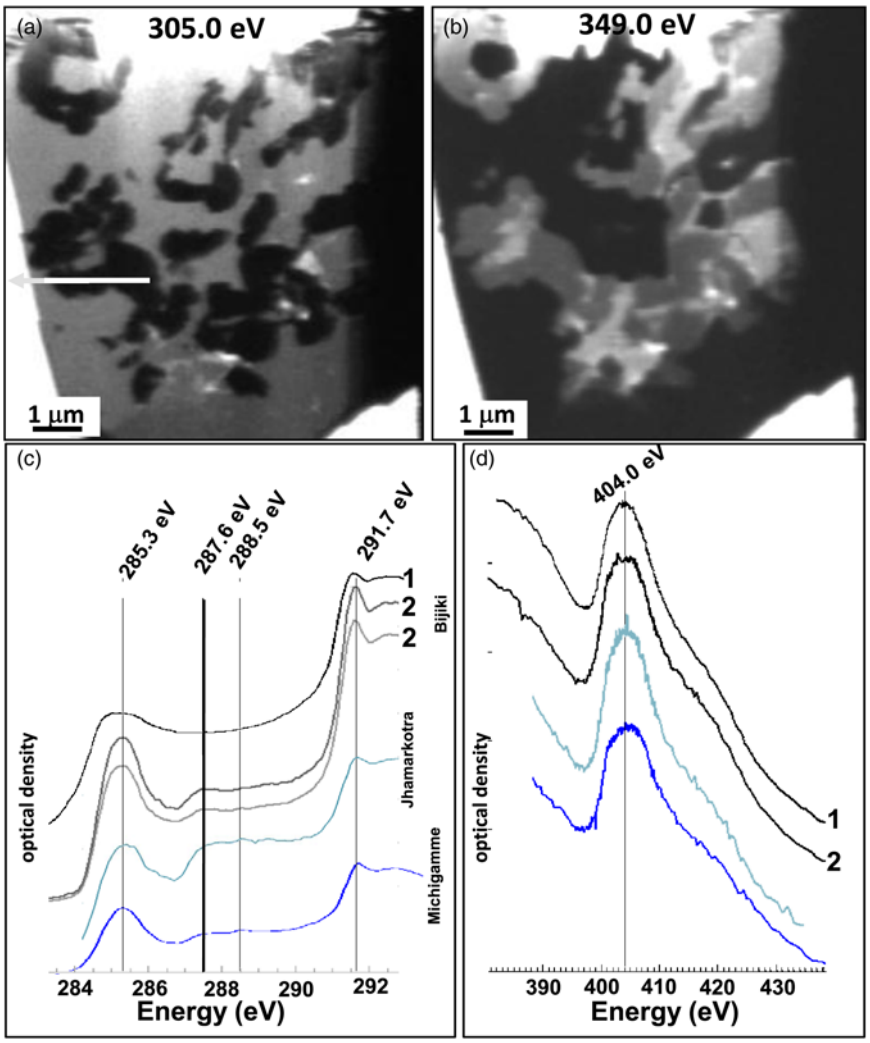

Fig. 5. X-ray absorption images and spectra of graphitic carbons with apatite. (**a**) 305.0 eV image, where graphitic carbon is the only phase strongly absorbing photons, hence appearing black. The white part of the arrow represents the line scan over the graphitic carbon (see also Fig. S4). (**b**) 349.0 eV image, where Ca-bearing phases are the strongest absorbers, showing the distribution of Ca in apatite (black), dolomite (black) and graphite in the FIB lamella. In this image, phyllosilicate is the brightest phase, closely associated with the distribution of graphitic carbon. XANES spectra at the (**c**) C-edge and (**d**) N-edge with major peaks identified. Graphitic carbons from Bijiki FIB lamella are labelled '1'; acid-insoluble Bijiki graphitic carbons are labelled '2'; the turquoise and blue spectra are from greenschist-facies phosphorite from the Jhamarkotra Formation (turquoise; sample UV0807 from Papineau *et al.* 2016) and from a phosphatic chert at the Big Eric's Crossing locality of the Michigamme Formation (blue; sample MA0708 from Papineau *et al.* 2017), respectively. Nitrogen was not detected by XANES in the phyllosilicate. (See also Fig. S4b–e for broader energy context.)

phase, whereas stilpnomelane is expected to have around 4.3 wt% Al, and hence this phyllosilicate mineral could also be minnesotaite or greenalite. This phyllosilicate is best seen in the contrast offered by He secondary electrons (Fig. 4c) and in X-ray images near the Ca_{2p}-edge (Fig. 5b). Although dolomite, apatite and silicate minerals are electrical insulators, we suggest that Fe in the phyllosilicate raises its conductivity at the nanometre scale, which yields higher contrast than apatite or dolomite in the secondary electron image from He-microscopy.

Compositions of graphitic carbon and associated phases

The carbon isotope composition of graphite was measured independently by three techniques, all in good agreement. Bulk powder (about 10 g) has $\delta^{13}C$ values (Papineau *et al.* 2010*b*) around −24.0‰, similar to three 2 mm diameter drilled spots (about 1 mg) that have $\delta^{13}C$ values between −23.4 and −21.4‰ (Fig. 1a), which shows relatively homogeneous compositions over centimetre scales. A pair of four 30 µm diameter spot analyses *in situ* by SIMS have $\delta^{13}C$ between −21.3 and −22.9‰ (Fig. 2a and b). This graphite layer analysed by SIMS is thus homogeneous with an average $\delta^{13}C_{gra}$ value ($n = 10$) of −21.7 ± 0.5‰ (1σ) (Table 2). It thus shows micron-scale homogeneous isotopic compositions over sub-millimetre layers of graphite. This rock is also known to have a $\delta^{13}C_{carb}$ value of −14.9‰ (Papineau *et al.* 2010*b*).

X-ray images acquired at energies above the photoabsorption energy for C show strong contrast from the graphitic carbon (Fig. 5a), but variable contrast is present within graphitic carbon as well, as shown by X-ray images acquired near the aromatic carbon ($1s \rightarrow \pi^*$) photoabsorption (*c.* 285 eV), especially for graphite completely embedded in apatite (Fig. S4b and c). Because the intensity of this π* peak is strongly dependent on the orientation of graphite lattice sheets (Rosenberg *et al.* 1986), this variable contrast at *c.* 285 eV indicates multiple oriented sub-domains of graphitic carbon, also referred to as highly aromatic carbon. Carbon-XANES spectra from the lamella show no molecular functional group (spectrum 1 in Fig. 5c), whereas some trace residual groups were detected on bulk acid-insoluble OM from the same sample with resolvable peaks at 287.6 and possibly at 288.5 eV (spectra 2 in Fig. 5c). This observation can hardly be attributed to younger contamination, which would be expected to have higher absorption, and is rather similar to the contemporary occurrences elsewhere in the Michigamme Formation and in the Jhamarkotra Formation. The weak peak at 287.6 eV could represent trace levels of aliphatic C–C bonds (Cody *et al.* 1996; De Gregorio *et al.* 2011; Bernard *et al.* 2012), whereas the peak at 288.5 eV represents the $1s \rightarrow \pi^*$ transition of carboxyl functional groups (Ishii & Hitchcook 1988; Cody *et al.* 1996; Boyce *et al.* 2002; Bernard *et al.* 2012) and/or interlayer states in the graphite structure (Fischer *et al.* 1991; Brandes *et al.* 2008). These two peaks are not unexpected for graphitic carbon metamorphosed at the amphibolite facies, as they are well resolved in acid-insoluble residues from the phosphatic Michigamme chert and Jhamarkotra stromatolite (Fig. 5c), both metamorphosed at the greenschist to upper greenschist facies. It is possible that the PCG could host most of the trace molecular functional groups detected in acid-insoluble residues (Fig. 5c).

The relatively low intensity of these peaks, however, is consistent with a trace residual abundance owing to metamorphism at the

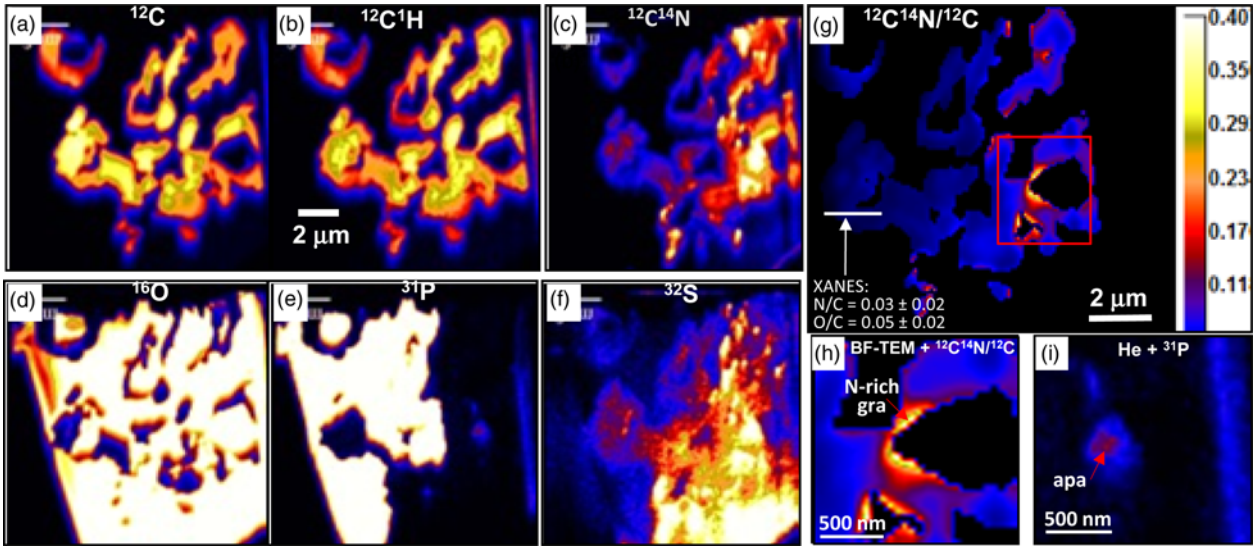

Fig. 6. Geochemical context of graphite associated with apatite and dolomite in Michigamme Fe-silicate BIF. (**a**–**f**) NanoSIMS secondary ion images. The distribution of graphite is visible in (**a**) $^{12}C^-$ and (**b**) $^{12}C^1H^-$ images, and the co-location of organic N is shown in (**c**). Dolomite-associated sulphate and the near absence of S in apatite can be seen in (**f**). (**g**) Map of the secondary $^{12}C^{14}N/^{12}C$ ratio calibrated for atomic N/C ratios using XANES data. (**h**) BF-TEM image superimposed by a semi-transparent $^{12}C^{14}N/^{12}C$ map and (**i**) He secondary electron image superimposed by semi-transparent ^{31}P, together showing N-rich graphitic carbon in contact with a nanoscopic grain of apatite. The location of these images is shown by the red box in (**g**).

amphibolite facies. All samples analysed by STXM also contain N with a peak centred at 404.0 eV, which could point to trace nitro-bearing groups (Cody *et al*. 2011; Alléon *et al*. 2016; Papineau *et al*. 2016), although the feature is broad enough that it could include contributions from many N-bearing organic functional groups (Fig. 5d). Other well-resolved peaks are absent from the Bijiki graphitic carbons N-XANES spectra, as well as from the greenschist- to upper greenschist-facies graphitic carbons of the Jhamarkotra and Michigamme formations (Fig. 5d; see Papineau *et al*. 2016). Peaks at 531.7 and 538.9 eV in the O-XANES spectrum may be consistent with C=O functional groups (Hitchcock & Biron 1980) (Fig. S4g). The low intensity of the O-edge relative to that for the phyllosilicate and apatite (Fig. S4g) is consistent with minor O in graphitic carbon. Molecular functional groups commonly found in graphitic carbons of biological origin from the lower greenschist-facies Gunflint Formation (De Gregorio *et al*. 2009; Alléon *et al*. 2016) and the greenschist- to upper greenschist-facies Jhamarkotra and Michigamme formations (Papineau *et al*. 2016, 2017) are therefore also preserved in the amphibolite-facies graphitic carbon of the Bijiki BIF, although at significantly lower levels and sometimes undetectable.

NanoSIMS secondary ion images reveal the presence of H, N, O and S within graphitic carbons (Fig. 6a–f). The H and N distributions, as seen in the $^{12}C^1H$ and $^{12}C^{14}N$ secondary ion images, match the graphitic carbon distribution shown by the ^{12}C secondary ion image (Fig. 6a–c). However, N appears more enriched in graphitic carbon embedded in dolomite than that in apatite (Fig. 6c). Low levels of N also occur in the phyllosilicate and therefore presumably N occurs as ammonium (NH_4^+) (Gruner 1937; Boyd 2001*a*, *b*). Oxygen was detected in all phases including in apatite, dolomite and phyllosilicate, although it was not clearly resolved in the graphitic carbon by nanoSIMS owing to the relative high flux of secondary $^{16}O^-$ ions from associated phases (Fig. 6d; Fig. S3a). Whereas no P was detected in dolomite (Fig. 6e), S was detected in relatively high levels in the dolomite, and in trace level in apatite, phyllosilicate and in graphitic carbons, where it is non-uniform and tends to form 'hot spots' (Fig. 6f). Structural and chemical heterogeneities are documented in nanoscopic spatial resolutions for all the microscopy techniques used and clearly show that well-ordered graphite and PCG occur in the FIB lamella and that they contain H, N, O and S (Figs 6 and 7).

Correlated microscopy can be achieved using semi-transparent and aligned overlays of different images, which can be useful to visualize correlations between nanoscopic chemical heterogeneities and specific mineral phases. This approach is taken here to show the following observations: (1) well-ordered graphite occurs as concentrically-layered and radiating flakes and linear books (Fig. 4d and e), whereas the associated PCG exhibits variable to random orientations (Fig. 7a); (2) the PCG is mixed with well-ordered graphite and a phyllosilicate resembling stilpnomelane (Fig. 7b); (3) highly aromatic domains are preferentially associated with PCG (Fig. 7c and l); (4) the Fe–Mg phyllosilicate contains N (Fig. 7d, e and k), probably as structural ammonium; (5) PCG contains preferential enrichments of H (Fig. 7g and n), N (Fig. 7h and k) and S (Fig. 7m). The picture that emerges from this complex and poly-crystalline mixture of graphitic carbons is one where the PCG contains the most compositional heterogeneities in the form of nanoscopic domains with elemental enrichments and where well-ordered graphite has more homogeneous compositions (Fig. 7o). Similar observations of heterogeneous S in graphitic carbon were previously reported in the Akilia Qp rock, in which nanoscopic sulphide inclusions occur (Papineau *et al*. 2010*a*), and are consistent with partial sulphidization of microorganisms during diagenesis, and the condensation and crystallization of S during metamorphism. We also note the presence of Mn in the apatite with around 0.2 wt% (Table 1), in phyllosilicates with 0.2–0.4 wt% (Table 1), in amphiboles with 1.8–2.7 wt% (Table 1) and in dolomite with 4.5–6.5 wt% (Table 1).

By fitting a combined CNO-XANES line spectrum collected along the edge of the FIB lamella to a linear combination of tabulated X-ray mass-absorption coefficients (Cody *et al*. 2008; Alléon *et al*. 2016) (Fig. S4e), we obtained atomic N/C and O/C ratios of 0.033 ± 0.019 and 0.051 ± 0.021, respectively. This method has been used before for the calibration of nanoSIMS elemental ratios in graphitic carbons (Alléon *et al*. 2015). An artefact in the intensity of transmitted X-rays between the C-EXAFS region and the N-edge caused a small shift in the spectrum and yielded a poor error of around ±60% for the estimated N/C of graphitic carbon. The STXM line-scan used for the calibration of nanoSIMS secondary ion ratios also had variable O intensities across the graphite (Fig. S4g), which suggests that more accurate calibrations could be achieved for smaller regions of the sample.

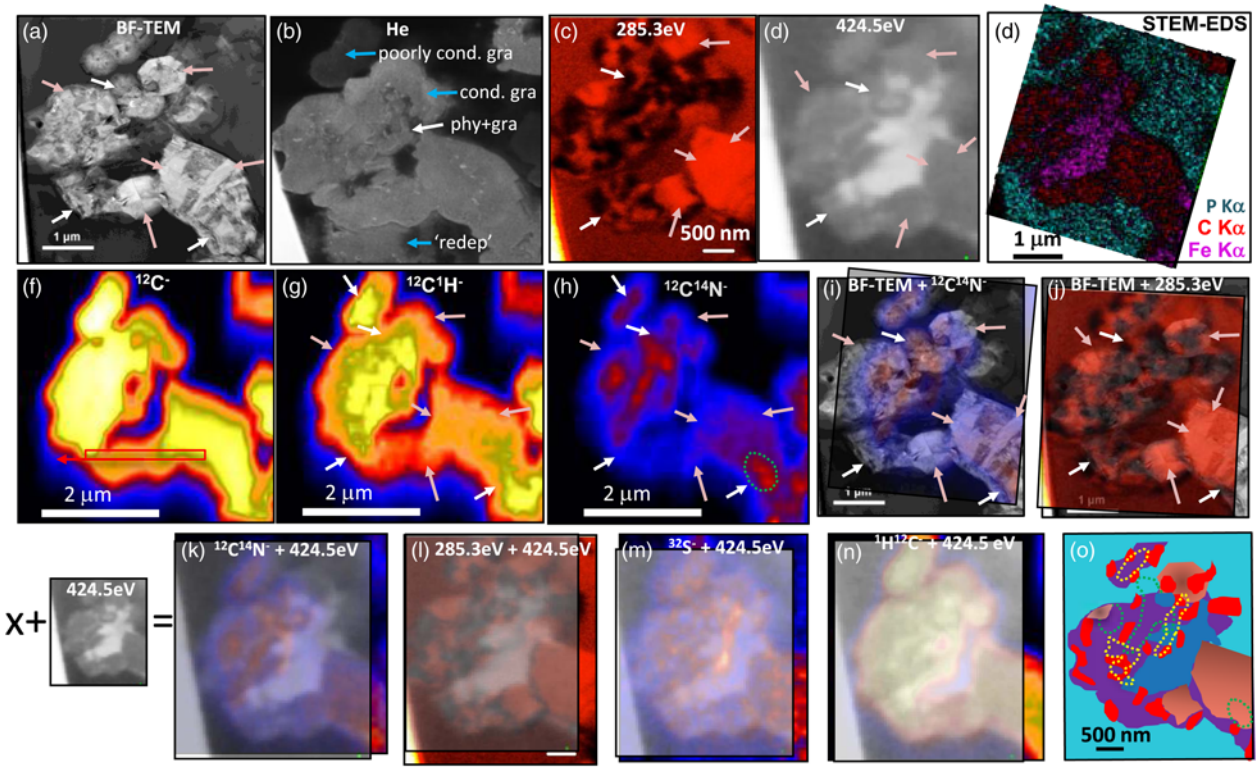

Fig. 7. Correlated microscopy of filamentous graphitic carbon from Michigamme BIF showing that disordered graphitic carbon and the well-ordered graphite both correlate to compositionally specific areas. (**a**) BF-TEM image of the region of interest showing well-ordered graphite (pink arrows) and disordered graphitic carbon (white arrows) as distinguished by sub-domains with variable to random orientations. (**b**) Secondary electron image from focused He beam showing phyllosilicate associated with graphitic carbon as well as highlighting the main contrast differences (blue arrows) in the He image attributed to the good electronic conductivity of re-deposition and parts of the graphitic carbon that are grounded (lightest grey) and poorly conductive graphite surrounded by apatite. X-ray images of graphite showing that (**c**) differences in absorption intensity at 285.3 eV are caused by the presence of variably oriented nanoscopic aromatic domains (black) in disordered graphitic carbon (white arrows), whereas well-ordered graphite (pink arrows) is best highlighted in the brightest red contrast. (**d**) At 424.5 eV, the association of well-ordered graphite (pink arrows) and disordered graphitic carbon (white arrows) is shown, with less homogeneous grey contrast for the latter. Phyllosilicate is the brightest phase. (**e**) STEM-EDS image of characteristic X-rays showing Fe in phyllosilicate, C in graphite and P in apatite. Negative secondary ion images of (**f**) ^{12}C, showing homogeneous graphitic carbon (the red box shows the pixels selected for inter-instrumental calibration of atomic N/C, using the corresponding STXM line scan; Alléon *et al.* 2015), and (**g**) $^{12}C^{1}H^{-}$ and (**h**) $^{12}C^{14}N^{-}$ showing nanoscopic heterogeneities within mostly the disordered graphitic carbon. Images superimposed on a correlated BF-TEM image are (**i**) a secondary ion image of $^{12}C^{14}N^{-}$ and (**j**) an X-ray image at 285.3 eV. Images superimposed over a correlated X-ray image at 424.5 eV, which shows phyllosilicate, include (**k**) secondary ion image for $^{12}C^{14}N^{-}$ showing nanoscopic zones of disordered graphitic carbon and phyllosilicate enriched in N, (**l**) X-ray image at 285.3 eV (in red) showing nanoscopic domains of aromatic carbon excluded from well-ordered graphite in the lower right, (**m**) secondary ion image for $^{32}S^{-}$ showing nanoscopic S-rich disseminations in the disordered graphitic carbon and a more homogeneous distribution in the well-ordered graphite, and (**n**) secondary ion image for $^{12}C^{1}H^{-}$ showing highest H levels in the disordered graphitic carbon. (**o**) Interpretative summary diagram of phases, which shows chemical zones (green dotted line, N-rich; yellow line, S-rich) preferentially located in the disordered graphitic carbon (turquoise, apatite; blue, phyllosilicate; purple, disordered graphitic carbon; pink shaded, concentric or aligned books of graphite; red, highly aromatic carbon).

Using the same line of pixels as that used for the XANES line-scan, we performed a calibration of the atomic N/C ratio measured by nanoSIMS to obtain a quantitative atomic N/C map from secondary ion images (Fig. 6g), which represents an improvement over previous semi-quantitative secondary ion images (Oehler *et al.* 2009, 2010; Wacey *et al.* 2012, 2013). In the lamella, the atomic N/C ratio is usually less than 0.04 (Fig. 6g), although there is a highly localized area with N/C ratio up to 0.4, which occurs on the edge of a nanoscopic apatite grain in the lamella (Fig. 6h and i). These compositional ratios are higher than previously published measurements by nanoSIMS up to 0.002 in three other graphite occurrences associated with apatite in this same rock and calibrated using a N-bearing graphite standard (Papineau *et al.* 2010*b*). These results show that N/C is heterogeneous over three orders of magnitude at sub-micron scales, although most commonly less than 0.04.

Auger electron spectroscopy (AES) measures the chemical composition of the first few atomic layers of the sample, hence atomically flattened surfaces are ideal for chemical analysis with this method (Fig. 8a). Auger electron spectra were acquired from two areas of the lamella for which TEM, STXM and nanoSIMS data were also acquired (Fig. 8b and c), but after re-thinning the surfaces by neon. Simultaneous SEM monitoring during the AES measurement ensured that the beam position did not shift significantly during acquisition (Schirmer *et al.* 2011). Both AES spectra contain electron peaks of C (*c.* 270 eV), O (*c.* 510 eV), Fe (*c.* 654 eV) and Ca (*c.* 290 eV), and the area marked in red also exhibits a clearly resolved N peak (*c.* 380 eV; Fig. 8c). Besides the occurrence of N in both graphitic carbon and phyllosilicate, Fe and Ca were also detected in both phases by AES. The spectrum for the phyllosilicate (blue curve in Fig. 8c) has a carbon peak area more than twice that for graphitic carbon (i.e. *c.* 63 at.% versus *c.* 25 at.%, respectively), which is interpreted as contamination of the surface by carbon re-deposition, and therefore these Auger data can only be used qualitatively for interpretations. Nevertheless, there are disordered sub-micron domains of graphite and phyllosilicate rich in Ca and N as detected by AES, which independently confirm some TEM, nanoSIMS and STXM observations (Figs 5b and 6c, g, Figs S2f and S4e), and point to co-crystallization with phyllosilicate.

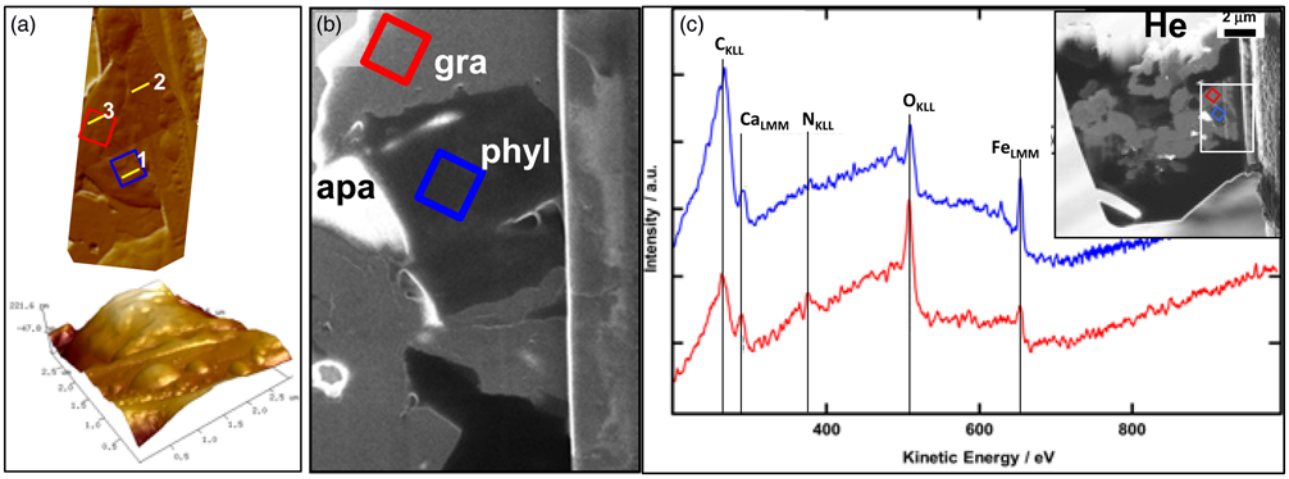

Fig. 8. Nanoscale topography of lamella of Michigamme graphite polished using a 400 fA beam of Ne ions and analysed by AFM and Auger spectroscopy. (**a**) AFM differential topographic height image of a section of the FIB lamella. Yellow lines indicate the locations of line profiles shown in Figure S5. (**b**) He secondary electron image of the area where two spots were analysed by Auger electron spectroscopy. (**c**) Two Auger spectra of the blue and red boxes in (**b**) with the localization in the lamella shown in the inset. These show the presence of C, N, O, Ca and Fe in both graphite and the phyllosilicate, although the relative intensity of the peaks is affected by re-deposition on the lamella.

Discussion

Fluid-deposition of apatite with graphitic carbons from carbonic fluids

Metamorphic recrystallization at the amphibolite facies in the Michigamme BIF yielded graphitic carbon associated with stilpnomelane included in and coating manganiferous apatite grains (Table 1) remobilized in a Mn-dolomite vein cross-cutting sedimentary layering (Fig. 1b). This petrographic context suggests that apatite was fluid-deposited earlier than dolomite and that it was assimilated along with OM from the sedimentary layers and transported in carbonic fluids. As bulk carbonate has a $\delta^{13}C$ value of −14.9‰ (Papineau *et al*. 2010*b*), much of the carbonate in dolomite can be interpreted to be the mineralized product of organic oxidation, as in other BIF (e.g. Heimann *et al*. 2010). NanoSIMS data also show that trace sulphate is present in dolomite (Fig. 6f), which suggests that it was present in the diagenetic environment and available for possible microbial or thermochemical sulphate reduction. The presence of Mn in dolomite, ankerite, apatite, stilpnomelane and grunerite from this rock (Table 1) is consistent with dolomite precipitation during decreased alkalinity in the presence of Ca^{2+}, Mg^{2+}, Mn^{2+} and Fe^{2+} during the remobilization of the carbonic fluids. This probably took place during peak metamorphism. The graphitic carbon inside the apatite and dolomite shows a slightly distorted structure, with expanded lattice spacings between 3.55 and 3.72 Å ($n = 6$), which explains the presence of a small D1 peak in the Raman spectra. Using the Raman spectrum acquired from this well-ordered graphite, the peak metamorphic temperature is estimated to be 567 ± 50°C (Fig. 3a) (Beyssac *et al*. 2002*a*), consistent with an indigenous source of OM. The presence of H, O, N and S heteroatoms in both well-ordered graphite and PCG is seen in nanoSIMS images, although it appears that the PCG hosts more trace heteroatoms, and possibly also carboxyl and aliphatic groups.

Based on the observation that the Raman spectra of the Michigamme graphite and PCG have the same D1, D2, G and 2D peak positions, we suggest that both these graphitic carbons have gone through the same metamorphic history. Comparable occurrences of distinct types of graphitic carbons associated with apatite occur in several other Precambrian BIF, and they are most common in highly metamorphosed rocks where fluid-deposition played an important role (Dodd *et al*. 2019). It is thus possible that both types of graphitic carbons were fluid-deposited and/or directly graphitized from biomass. Hence the PCG is unlikely to represent younger migrated organic matter. This also unlikely because there are no suitable Phanerozoic source rocks in the Michigan Upper Peninsula, and arguments for syngenetic oil generation and migration in the late Paleoproterozoic sedimentary rocks of the Michigamme Formation have been based on vitrinite reflectance, heteroatom contents and carbon isotope ratios of 'anthraxolite' pyrobitumen (Mancuso *et al*. 1989). Hence, we find it more likely that the PCG and well-ordered graphite in the Raman spectra differ most probably by having variable levels of functional groups and heteroatoms, and variable ordering possibly owing to metamorphic crystallization, whereas graphite probably represents both fluid-deposited and directly graphitized sedimentary organic matter formed during peak metamorphism.

Oxidized products of biomass include carbonate and phosphate, which could have initially precipitated as carbonate–apatite layers between silicate- and magnetite-rich BIF layers. Thermal metamorphism during the Penokean Orogeny then caused the remobilization of Mn-dolomite into veins, the fluid-deposition of manganiferous apatite (Table 1), the crystallization of graphitic carbon containing aliphatic groups, the fluid-deposition of graphite spherulites, and the crystallization of stilpnomelane, grunerite and anthophyllite from ferric–ferrous and manganiferous clay precursors (Table 1). The presence of Mn in the Michigamme BIF is consistent with a syndepositional hydrothermal–sedimentary source, the same source as Fe, and akin to other manganiferous Precambrian BIF occurrences (Roy 2006).

Assessing the possible non-biological origins of graphitic carbon and associated minerals

In the context of the search for evidence of early life in metamorphosed sedimentary rocks, the null hypothesis should be evaluated, which means that all possible known non-biological processes should be considered before a biological conclusion can be established. Microscopic concentrically-layered and radial flakes of graphite preserved in the Bijiki BIF (Fig. 4d) probably formed in part as a result of the non-biological fluid-deposition of graphite, from the spontaneous reaction of CO_2 and CH_4 either from non-biological mantle sources or from decomposed microbial biomass (next section). They have a pseudo-hexagonal habit different from that of millimetric graphite 'spherulites' from the Pogranichnoe

carbonatite formed from non-biological carbon (Doroshkevitch *et al*. 2007) and from alkaline pegmatite in the Kola Peninsula with a hydrothermal origin (Jaszczak *et al*. 2007). Graphite spherulites in both of these Russian occurrences are formed by radially aligned graphite needles and tubes, whereas the Michigamme graphite forms distinct concentrically aligned books. In addition, the non-biological graphite from Pogranichnoe and Kola also co-occurs with apatite, showing that these mineral associations can also be non-biological in origin (Doroshkevitch *et al*. 2007; Jaszczak *et al*. 2007). Other mantle-fluid processes can also produce non-biological OM associated with apatite as in the case of the Chassigny dunite from Mars where these associated phases have been reported (Papineau 2012). Instead, the Bijiki graphitic carbon appears unique to sedimentary lithologies and is similar to graphite filaments from the Jingangku Fm in the *c.* 2.5 Ga Wutai Complex of China (Schiffbauer *et al*. 2007). However, the association of apatite with graphitic carbon can occur through non-biological processes and hence the null hypothesis cannot be rejected for this mineral association nor for the morphology of some Michigamme graphitic carbon.

To further test the null hypothesis, possible non-biological sources of complex OM could be remobilized to form mantle carbon with an expected $\delta^{13}C$ value around −5‰, characteristic of the upper mantle (Horita 2005). Graphite can be spontaneously fluid-deposited during the reduction of CO_2 and the oxidation of CH_4 in aqueous fluids (Rumble 2014), which has been suggested to lead to the deposition of non-biological graphitic carbon in basalt and pyroxenite on Mars (Steele *et al*. 2012). Fischer–Tropsch Type (FTT) synthesis can also lead to the formation of short-chain alkanes through catalysis by Cr- and Fe-bearing spinels, although Ni-sulphides tend to favour the production of CH_4 over short alkanes (Foustoukos & Seyfried 2004). Experiments of FTT synthesis show that organic carbon can be significantly depleted in ^{13}C by up to 36‰ (McCollom & Seewald 2007), although in modern hydrothermal systems FTT carbon is not usually depleted by more than 16‰ (Proskurowski *et al*. 2008). In addition, FTT experiments with variably complex reactants show that various organic compounds containing C, H, O, N and S can be synthesized non-biologically under hydrothermal conditions (Rushdi & Simoneit 2004). Because the hydrothermally influenced environment of the Michigamme BIF is a plausible site for hydrocarbons generated by FTT reactions, the null hypothesis for the isotopic and elemental composition of the graphitic carbon cannot be entirely rejected.

It has also been suggested that Mn-, Mg-, Ca- and Fe-bearing carbonic fluids reacted to form non-biological graphite associated with apatite grains in metasomatically altered carbonate rocks from the Eoarchean Isua Supracrustal Belt (Lepland *et al*. 2002). The decarbonation of siderite occurs at temperatures above 450°C and can produce graphite along with magnetite and CO_2 (French 1971; McCollom 2003), which could conceivably have re-precipitated as carbonate. Dolomitic carbonate has been proposed as a biosignature (Nutman *et al*. 2010), although recent carbonation experiments show that clay minerals such as illite and montmorillonite can stimulate the non-biological precipitation of proto-dolomite under ambient conditions (Liu *et al*. 2019). Similarly, NH_4^+ in phyllosilicates has also been proposed to be a biosignature (Boyd 2001*b*), but it could have been sourced from hydrothermal fluids, possibly from non-biological sources such as N_2 reduction with H_2S (Schoonen & Xu 2001) or the reduction of NO_3^- or NO_2^- with Fe–Ni metals (Summers & Chang 1993; Brandes *et al*. 1998; Smirnov *et al*. 2008). Hence there are known non-biological processes in hydrothermal and metamorphic systems that can result in the precipitation of dolomite with graphitic carbon as well as ammoniated phyllosilicates and therefore the null hypothesis for these biosignatures cannot be rejected.

In summary, there are processes under hydrothermal conditions that may produce purely non-biological OM with ^{13}C-depletion, trace elements of H, N, O and S, and molecular functionalities, or associations with apatite or ammoniated phyllosilicates. However, these non-biological scenarios can explain only some characteristics of the Michigamme graphite and associated minerals; the key fact remains that all observations combined point to a biological origin. A number of non-biological processes can produce the features reported here, but those mechanisms have to converge to coherently explain all the combined key lines of evidence: (1) the geological context in a BIF unit, known to have contemporary versions with prolific stromatolites and microfossils; (2) the presence of syngenetic graphitic carbon with an expanded crystalline structure consistent with metamorphic history; (3) the observed carbon isotope homogeneity, heteroatom heterogeneity and trace molecular compositions; (4) the association of graphitic carbon with NH_4^+-bearing phyllosilicate inside apatite, and with sulphate-bearing ^{13}C-depleted dolomite. Indeed, non-biological processes are unlikely to produce all these observed elemental, isotopic, molecular, structural and mineralogical features documented here together for the metamorphosed Michigamme BIF. Hence, because life had also been present throughout the late Paleoproterozoic and since at least the Eoarchean, we conclude that a microbial origin is the simplest and most likely explanation for the observed compositions of graphitic carbons and their associated minerals.

The preservation of metamorphosed biological signatures in graphitic carbon

In the Michigamme Formation, the age of peak metamorphism was around 1.833 Ga with the intrusion of various plutons and 1.830 Ga with regional metamorphism (Schulz & Cannon 2007). The origin of the carbon in the Michigamme graphitic carbon must therefore be indigenous and syngenetic, as is the case for graphite in the Biwabik Formation in northern Minnesota (French 1964). The degree of crystallinity of graphitic carbon associated with apatite in the Michigamme silicate BIF was significantly modified by thermal metamorphism as seen in the Raman spectrum with a low G peak position and a weak D1 peak (Fig. 3a), commonly observed in metamorphosed graphitic carbon (Beyssac *et al*. 2002*a*, *b*).

We now consider that the Michigamme graphite represents the metamorphosed remains of microorganisms and that the most graphitized micron-size domains (e.g. Fig. 4d and e) represent microbial biomass that could have been partly fluid-deposited (Rumble 2014). This would have occurred during thermal metamorphism, possibly from dehydration reactions involving phyllosilicate precipitation, CH_4 cracked from alkanes, and CO_2 from oxidized and kerogen decarboxylated ion. No fluid inclusions have been observed so far in the specimens. Direct graphitization of biomass is proposed for the graphitic carbon associated with phyllosilicate (Fig. 7a and b). The graphitic carbon seen in BF-TEM images typically has nanoscopic inclusions of highly aromatic carbon (as seen from the most opaque domains at 285.3 eV; Fig. 7c, j and l), and contains heterogeneities of N, S and H (Fig. 7g, h and m). We observed no nanoscopic inclusions of sulphide inside the graphite (Fig. S2k–o). Hence, these observations are consistent with nanoscopic chemical heterogeneities observed in biological carbon from chert metamorphosed at sub-greenschist facies in the Gunflint Fm (Wacey *et al*. 2013). Organic matter from the Gunflint chert also contains heteroatoms of N, O, P and S as well as aromatic alcohol, phenol and carboxylic acid functional groups (De Gregorio *et al*. 2009; Alléon *et al*. 2016). Residual heteroatoms are largely preserved at the greenschist facies, where H/C is typically between 0.1 and 0.5 (Hayes *et al*. 1983; Watanabe *et al*. 1997). The above observations are also consistent with trace element compositions in metamorphosed graphitic carbons from

Table 3. *Comparison of mineralogical and geochemical data relevant for biosignatures between the Bijiki Fe-silicate BIF and the Akilia Qp rock*

	Amphibolite facies Bijiki Fe-silicate BIF	Granulite facies Akilia Qp rock
Age	*c.* 1.85 Ga[1]	>3.83 Ga[2]
Metamorphic temperature	$T = 567 \pm 50$°C[3]	$T > 635$°C[4]
Mineralogy	Grunerite, magnetite, quartz, dolomite, stilpnomelane, chlorite, pyroxene, biotite, graphite, apatite, pyrrhotite, pyrite[3]	Quartz, pyroxene (hedenbergite-ferrosilite), magnetite, grunerite-hornblende, calcite, apatite, graphite, pyrrhotite, chalcopyrite, pentlandite[4]
Specific mineral associations with graphitic carbon	Apatite, dolomite, magnetite, stilpnomelane, grunerite, chlorite, pyrrhotite, quartz[3]	Apatite, calcite, magnetite, hornblende-grunerite, chalcopyrite, pyrrhotite, quartz[4]
Evidence for fluid remobilization	Apatite grains occur in carbonate veins[3]	Apatite occurs in coarse quartz with fields of fluid inclusions[4,5]
Petrography of apatite	Concentrated in some sedimentary layers[6]	Concentrated in some layers of coarse quartz[6]
$\delta^{13}C_{carb}$	−14.9‰[6]	−3.3. to −5.5‰[6]
$\delta^{13}C_{gra}$ (in situ)	−21.3 to −22.9‰[3]	−4.1 to −49.0‰[6,7]
$\delta^{13}C_{gra}$ (bulk)	−21.7 to −24.3‰[3,6]	−12.6 to −23.6‰[6]
Crystallinity of graphitic carbon	D-bands between 1346 and 1353 cm^{-1} (FWHM between 41 and 51 cm^{-1} and between 82 and 85 cm^{-1}) and G-bands between 1574 to 1581 cm^{-1} (FWHM between 41 and 77 cm^{-1})[3,6]	D-bands between 1344 and 1358 cm^{-1} (FWHM between 22 and 29 cm^{-1}) and G-bands between 1573 to 1581 cm^{-1} (FWHM between 10 and 46 cm^{-1}); presence of curled graphite structures[4]
d-spacing of graphitic carbon	3.55–3.72 Å[3]	3.41–3.64 Å[4]
Atomic N/C in graphitic carbon	10^{-4} to 10^{-1} [3,6]	10^{-6} to 10^{-4} [6]
Heteroatoms in graphitic carbon	H, N, O, S, P, Ca, Fe[3,6]	H, N, O, S, P, Fe[6]
Petrography of heteroatoms in graphitic carbon	Forms sub-micrometer-size hot spots[3,6]	Forms sub-micrometer-size hot spots[6]
Molecular functional groups	Aliphatic and carboxyl (both minor)[3]	None detected[3]

[1]Schulz & Cannon (2007).
[2]Manning *et al.* (2006).
[3]This work.
[4]Papineau *et al.* (2010*a*).
[5]Lepland *et al.* (2010).
[6]Papineau et al. (2010*b*).
[7]Mojzsis *et al.* (1996).

stromatolitic phosphorite and pelite including black shale in the contemporary Aravalli Group, India, which have Raman spectra with significant D1 peaks (fig. 7 of Papineau *et al.* 2009) and C-XANES spectra often with resolved peaks for carboxyl, aliphatic, nitrile and nitro functional groups (fig. 11 of Papineau *et al.* 2016).

Hence, all characteristics of graphitic carbon and associated minerals in the Michigamme Formation are independently consistent with a biological source of carbon from the original depositional environment, and they include the following: (1) Raman peaks for graphitic carbon consistent with the metamorphic history and silicate mineral assemblages (Fig. 3); (2) the common filamentous graphite morphology (Fig. 2d) never observed in igneous rocks, where graphite usually has geometric crystal habits (Jaszczak *et al.* 2003, 2007); (3) the slightly expanded graphite lattice spacings (Fig. 4f) consistent with crystallization of an organic precursor with heteroatoms; (4) the trace levels of molecular functional groups in graphitic carbon, which are consistent with the independently detected presence of H, N, O and Ca (Figs 5c, d, 6a–f and 8c, Fig. S4e), and similar to what was observed in kerogen from the Gunflint Fm (Alléon *et al.* 2016); (5) the heterogeneous distribution of N and S, which are concentrated over areas <500 nm in size (Fig. 7k and m), similar to heterogeneous N distributions in OM from the Gunflint Fm (Wacey *et al.* 2013); (6) the ^{13}C-depleted Mn–Fe dolomite (down to −14.9‰) in veins that most probably sourced carbonate from diagenetically oxidized biomass (Papineau *et al.* 2010*b*), similar to other BIF (Heimann *et al.* 2010); (7) the systematic association of graphitic carbon with C- and N-bearing phyllosilicate (Fig. 7h and k), which may contain NH_4^+ of biological origin (Boyd 2001*b*) such as in coeval BIF from Minnesota (Blake 1965); (8) the co-occurrence with manganiferous dolomite, apatite, stilpnomelane and grunerite (Table 1), which indicate precipitation from fluids with hydrothermally sourced metals (Roy 2006); (9) fractionated $\delta^{13}C$ values consistent with a metamorphic overprint on the signature of photoautotrophic biomass (Table 2) (Desmarais 2001). These indications point to the Michigamme graphitic carbons having a biological origin, probably dominated by oxygenic photosynthesis, and having formed variably crystallized graphitic carbon during metamorphism (Mancuso *et al.* 1989). Fluid-deposition during the retrograde phase of peak metamorphism could also explain why there is both graphite and PCG in this rock, which could have formed from devolatilized biomass and reaction products such as CO_2 and CH_4.

The compositions of the Michigamme graphitic carbon are those expected for microbial biomass metamorphosed at the amphibolite facies and thus include trace levels of biological element heterogeneities and carbon isotope distributions that are homogeneous from centimetre to micrometre scales. Heating experiments on acritarch microfossils composed of OM have shown that residual ketone and aldehyde functional groups can be preserved after several days of exposure to temperatures at 500°C, and also that recognizable biological structures are best preserved under anoxic metamorphic conditions, but also under oxic conditions (Schiffbauer *et al.* 2012). These details are important because they demonstrate key characteristics of kerogen metamorphosed at low metamorphic grades and lead to the conclusion that some elemental and molecular characteristics of degraded biomass can be preserved at high metamorphic grades (Boyce *et al.* 2002; Bernard *et al.* 2007, 2009).

In summary for the Michigamme BIF, the oxidative and thermal degradation of photoautotrophic microbial biomass with silicate-rich ferruginous sediments produced kerogen, apatite, dolomite with sulphate, sulphide, ferric–ferrous oxides such as hydromagnetite, and phyllosilicates such as greenalite and stilpnomelane. These diagenetic minerals were then crystallized along with PCG and graphite during prograde metamorphism, whereas PCG can be interpreted to have formed from thermally cracked products that were solubilized, remobilized and fluid-deposited during amphibolite-facies metamorphism, but after peak metamorphism. These processes would have begun with precursor biomass mixed with silica and ferruginous clays, and are now preserved as a complex mixture of fluid-deposited graphite and PCG from residual biomass, mixed with apatite, Mn–Fe-dolomite with sulphate, and phyllosilicate with NH_4^+, and associated with mineral reaction products from diagenesis and metamorphism including magnetite, pyrrhotite, biotite, chlorite and grunerite. However, examples from other highly metamorphosed Fe-silicate BIF and graphitic schists should also be rigorously tested by studying graphite petrology and geochemistry.

Implications for the Akilia Qp rock

Comparisons with graphite from the granulite-facies Akilia Qp rock should reveal a more extreme effect of metamorphism above 640°C on OM with similar original characteristics. Although graphite from the Akilia Qp rock has characteristics consistent with a biological origin, the geochemical pathways of fluid-deposited graphite with apatite are unknown for such high-temperature metamorphism, and thus uncertainties persist for possible contributions from non-biological sources of carbon in the Akilia graphite. The key observations for Akilia graphite are listed in Table 3 (Papineau *et al.* 2010*a*, *b*) and include the following: (1) its common association as coatings on apatite in linear fields of fluid inclusions in coarse quartz, suggesting precipitation from fluids; (2) its slightly expanded graphite lattice spacings, consistent with the presence of heteroatoms; (3) its heterogeneous distribution of N and S, consistent with similar observations in younger metamorphosed graphitic carbons; (4) its co-occurrence with ^{13}C-depleted calcite, consistent with some oxidized organic matter; (5) its ^{13}C-depleted composition, not inconsistent with isotopic fractionation of biomass metamorphosed at the granulite facies; (6) the presence of curled graphite structures, consistent with granulite-facies thermal metamorphism; (7) the absence of molecular functional groups in C-XANES spectra that confirm the graphitic nature of the carbon (Papineau *et al.* 2010*a*, *b*), and consistent with a complete removal of residual functional groups at the granulite facies. The PCG has spectral and compositional similarities to younger graphitic carbons of biological origin (e.g. from the Aravalli Supergroup; Papineau *et al.* 2009, 2016), and C-XANES spectra for bulk acid-insoluble organic matter in the Bijiki BIF suggest that it could be the host of trace residual functional groups and heteroatoms.

Fluid-deposited graphitic carbon can form from microbial biomass, possibly from thermally cracked alkanes and decarboxylated kerogen, and could be associated with ^{13}C-depleted carbonate and hydrated minerals, as well as fluid inclusions in quartz that contain CH_4 and CO_2 (Lepland *et al.* 2010). Collectively, the new observations demonstrate the preservation of molecular, elemental and isotopic biosignatures in graphitic carbon metamorphosed at the amphibolite facies, and strengthen the case for the biological origin of carbon in graphite from the Akilia Qp rock. Although some workers have suggested that the protracted metamorphic history of the Akilia Qp rock precludes any biogenic interpretation and makes it 'impossible' to prove a biological origin (Lepland *et al.* 2010), progress can still be achieved as demonstrated in the present study. The new observations of graphitic carbons associated with fluid-deposited apatite from the Michigamme Formation show highly similar compositions (Table 3), consistent with slightly lower metamorphic temperatures than in the Akilia Qp rock. In both rocks, apatite grains tend to be concentrated in layers or bands, which is further consistent with the biological origin of apatite-rich layers associated with ^{13}C-depleted carbonate and organic matter in the Neoarchean Temagami and Brockman Fe-silicate BIF (Dodd *et al.* 2019). A continuum of the key characteristics of graphitic carbon observed in biomass metamorphosed at the amphibolite and granulite facies is thus established for the first time.

Conclusions

In the amphibolite-facies Michigamme Fe-silicate BIF, the diagenetic oxidation of biomass along with metamorphism at temperatures in excess of 550°C produced the precursors to the mineralization of Mn–Fe dolomite, graphitic carbons, apatite and sulphides as well as various ferric–ferrous phases including magnetite, anthophyllite, grunerite and phyllosilicates. Apatite associated with graphitic carbon in this silicate BIF was fluid-deposited from remobilized carbonic fluids that also contained highly polyaromatic hydrocarbons from oxidized and decarboxylated kerogen. The preservation of graphitic carbon as micron-size coatings and inclusions in apatite grains is probably the result of co-precipitation of apatite, carbonate and graphitic carbon from phosphatic and carbonic fluids under amphibolite-facies temperatures. The graphitic carbon contains trace levels of heterogeneous H, N, O and S as well as trace amounts of aliphatic and possibly carboxyl groups. Carbon isotope ratios of graphite layers are homogeneous with a $\delta^{13}C$ around −22‰ at centimetre to micrometre scales, which shows that carbon isotopes were fractionated during prograde metamorphism. Graphite also co-occurs with fine-grained ammoniated phyllosilicate and is embedded in manganiferous apatite and sulphate-bearing dolomite. Because all the expected elemental, isotopic, molecular, mineralogical and morphological biosignatures of degraded microorganisms occur in the Bijiki BIF, the reported data are most consistent with a biological origin. There are also no known non-biological graphitic carbons with comparable petrographic distribution, mineral associations and geochemical composition, such that the null hypothesis can be reasonably rejected for our combined observations. However, none of the null hypotheses for each independent line of evidence evaluated on its own can be rejected.

These observations shorten the observational gap of graphitic carbon from biological origin between the amphibolite and granulite facies. In the Eoarchean Akilia Qp rock, graphite occurs in several forms such as apatite coatings (Papineau *et al.* 2010*a*), as hydrothermal mineral associations with calcite (Papineau *et al.* 2010*a*) and as fluid inclusions that also contain CO_2 and CH_4 (Lepland *et al.* 2010). Graphite coatings on apatite grains from the Akilia Qp rock could have formed from recrystallized biomass (Mojzsis *et al.* 1996; Nutman & Friend 2006; McKeegan *et al.* 2007; Papineau *et al.* 2010*b*), and our new data further support this interpretation by filling the observational gap between well-characterized kerogen from greenschist-facies metamorphism (De Gregorio *et al.* 2009; Wacey *et al.* 2013; Alléon *et al.* 2016; Papineau *et al.* 2016, 2017), and more highly metamorphosed graphitic carbons at amphibolite facies (French 1964; Beyssac *et al.* 2002*b*; Schiffbauer *et al.* 2007). Graphitic carbon associated with apatite, dolomite, ferric–ferrous oxides and silicates can constitute a solid biosignature in metamorphosed sedimentary rocks if (1) the geological context is permissive both from the metamorphic history and the inferred depositional environment and (2) the mineralogical, elemental, isotopic and molecular signatures of life are preserved with or in graphitic carbon and their abundances and distributions are consistent with the metamorphic grade and analogous

occurrences. This robust evaluation of the geological transformation of biomass through thermal metamorphism further paves the way to search for biosignatures in other ancient environments, including ancient planetary surfaces such as that of Mars.

Acknowledgements We thank M. Humphrey for access to drill cores in Marquette, R. Hazen for providing the BH graphite from Sri Lanka for SIMS analyses, M. L. Fogel for access to the CF-EA-IRMS system, R. Stroud and S. Huo for assistance with FIB nano-fabrication, and B. French for discussions on metamorphic graphite. The EPSRC supported the acquisition of the Zeiss Orion NanoFab microscope used in this work (grant # EP/K024701/1 to P. Warburton). STXM data were acquired at the Advanced Light Source, which is supported by the Director, Office of Science, Office of Basic Energy Sciences of the US Department of Energy (under Contract No. DE-AC02-05CH11231). This paper benefited from four constructive reviewers and subject editor P. Donoghue, who are all thanked for their criticism that improved this paper.

Funding D.P. acknowledges financial support from the University College London, Carnegie Institution for Science, NASA Astrobiology Institute (grant # NNA04CC09A), NASA Exobiology and Evolutionary Biology Program (grant # NNX08AO16G), NASA Early Career Fellowship Program (grant # NNX12AG14G) and Carnegie of Canada.

Scientific editing by Philip Donoghue

References

Alléon, J., Bernard, S., Remusat, L. & Robert, F. 2015. Estimation of nitrogen-to-carbon ratios of organics and carbon materials at the submicrometer scale. *Carbon*, **84**, 290–298, https://doi.org/10.1016/j.carbon.2014.11.044

Alléon, J., Bernard, S. *et al.* 2016. Molecular preservation of 1.88 Ga Gunflint organic microfossils as a function of temperature and mineralogy. *Nature Communications*, **7**, article number 11977, https://doi.org/10.1038/ncomms11977

Barghoorn, E.S. & Tyler, S.A. 1965. Microorganisms from the Gunflint chert. *Science*, **147**, 563–575, https://doi.org/10.1126/science.147.3658.563

Bernard, S. & Papineau, D. 2014. Graphitic carbons and biosignatures. *Elements*, **10**, 435–440, https://doi.org/10.2113/gselements.10.6.435

Bernard, S., Benzerara, K., Beyssac, O., Menguy, N., Guyot, F., Brown, G.E. & Goffe, B. 2007. Exceptional preservation of fossil plant spores in high-pressure metamorphic rocks. *Earth and Planetary Science Letters*, **262**, 257–272, https://doi.org/10.1016/j.epsl.2007.07.041

Bernard, S., Benzerara, K., Beyssac, O., Brown, G.E., Grauvogel Stamm, L. & Duringer, P. 2009. Ultrastructural and chemical study of modern and fossil sporoderms by Scanning Transmission X-ray Microscopy (STXM). *Review of Palaeobotany and Palynology*, **156**, 248–261, https://doi.org/10.1016/j.revpalbo.2008.09.002

Bernard, S., Wirth, R., Schreiber, A., Schulz, H.-M. & Horsfield, B. 2012. Formation of nanoporous pyrobitumen residues during maturation of the Barnett Shale (Fort Worth Basin). *International Journal of Coal Geology*, **103**, 3–11, https://doi.org/10.1016/j.coal.2012.04.010

Beyssac, O., Goffe, B., Chopin, C. & Rouzaud, J.N. 2002*a*. Raman spectra of carbonaceous material in metasediments: a new geothermometer. *Journal of Metamorphic Geology*, **20**, 859–871, https://doi.org/10.1046/j.1525-1314.2002.00408.x

Beyssac, O., Rouzaud, J.-N., Goffé, B., Brunet, F. & Chopin, C. 2002*b*. Graphitization in a high-pressure, low-temperature metamorphic gradient: a Raman microspectroscopy and HRTEM study. *Contributions to Mineralogy and Petrology*, **143**, 19–31, https://doi.org/10.1007/s00410-001-0324-7

Blake, R.L. 1965. Iron phyllosilicates of the Cuyuna district in Minnesota. *American Mineralogist*, **50**, 148–169.

Boyce, C.K., Cody, G.D. & Feser, M. 2002. Organic chemical differentiation within fossil plant cell walls detected with X-ray spectromicroscopy. *Geology*, **176**, 1–30, https://doi.org/10.1130/0091-7613(2002)030<1039:OCDWFP>2.0.CO;2

Boyd, S.R. 2001*a*. Nitrogen in future biosphere studies. *Chemical Geology*, **176**, 1–30, https://doi.org/10.1016/S0009-2541(00)00405-8

Boyd, S.R. 2001*b*. Ammonium as a biomarker in Precambrian metasediments. *Precambrian Research*, **108**, 159–173, https://doi.org/10.1016/S0301-9268(00)00162-5

Brandes, J.A., Boctor, N.Z., Cody, G.D., Cooper, B.A., Hazen, R.M. & Yoder, H.S. 1998. Abiotic nitrogen reduction on the early Earth. *Nature*, **395**, 365–367, https://doi.org/10.1038/26450

Brandes, J.A., Cody, G.D., Rumble, D., Haberstroh, P., Wirick, S. & Gelinas, Y. 2008. Carbon K-edge XANES spectromicroscopy of natural graphite. *Carbon*, **46**, 1424–1434, https://doi.org/10.1016/j.carbon.2008.06.020

Carrigan, W.J. & Cameron, E.M. 1991. Petrological and stable isotope studies of carbonate and sulfide minerals from the Gunflint Formation, Ontario: evidence for the origin of early Proterozoic iron-formation. *Precambrian Research*, **52**, 347–380, https://doi.org/10.1016/0301-9268(91)90088-R

Cody, G.D., Botto, R.E., Ade, H. & Wirick, S. 1996. The application of soft X-ray microscopy to the *in-situ* analysis of sporinite in coal. *International Journal of Coal Geology*, **32**, 69–86, https://doi.org/10.1016/S0166-5162(96)00031-6

Cody, G.D., Alexander, C.M.O.'D. *et al.* 2008. Organic thermometry for chondritic parent bodies. *Earth and Planetary Science Letters*, **272**, 446–455, https://doi.org/10.1016/j.epsl.2008.05.008

Cody, G.D., Heying, E., Alexander, C.M.O.'D., Nittler, L.R., Kilcoyne, A.L.D., Sandford, S.A. & Stroud, R.M. 2011. Establishing a molecular relationship between chondritic and cometary organic solids. *Proceedings of the National Academy of Sciences of the USA*, **108**, 19171–19176, https://doi.org/10.1073/pnas.1015913108

De Gregorio, B.T., Sharp, T.G., Flynn, G.J., Wirick, S. & Hervig, R.L. 2009. A biogenic origin for Earth's oldest putative microfossils. *Geology*, **37**, 631–634, https://doi.org/10.1130/G25683A.1

De Gregorio, B.T., Sharp, T.G., Rushdi, A.I. & Simoneit, B.R.T. 2011. Bugs or gunk? Nanoscale methods for assessing the biogenicity of ancient microfossils and organic matter. *In*: Golding, S.D. & Glikson, M. (eds) *Earliest Life on Earth: Habitats, Environments, and Methods of Detection*. Springer, Dordrecht, 239–289.

Desmarais, D. 2001. Isotopic evolution of the biogeochemical carbon cycle during the Precambrian. *In*: Valley, J.W. & Cole, D. (eds) *Stable Isotope Geochemistry*. Mineralogical Society of America and Geochemical Society, Reviews in Mineralogy and Geochemistry, **43**, 555–578, https://doi.org/10.2138/gsrmg.43.1.555

Dodd, M.S., Papineau, D. *et al.* 2019. Widespread occurrences of variably crystalline ^{13}C-depleted graphitic carbons in banded iron formations. *Earth and Planetary Science Letters*, **512**, 163–174, https://doi.org/10.1016/j.epsl.2019.01.054

Doroshkevitch, A.G., Wall, F. & Ripp, G.S. 2007. Magmatic graphite in dolomite carbonatite at Pogranichnoe, North Transbaikalia, Russia. *Contributions to Mineralogy and Petrology*, **153**, 339–353, https://doi.org/10.1007/s00410-006-0150-z

Farquhar, J., Hauri, E. & Wang, J. 1999. New insights into carbon fluid chemistry and graphite precipitation: SIMS analysis of granulite facies graphite from Ponmudi, South India. *Earth and Planetary Science Letters*, **171**, 607–621, https://doi.org/10.1016/S0012-821X(99)00177-6

Fischer, D.A., Wentzcovitch, R.M., Carr, R.G., Continenza, A. & Freeman, A.J. 1991. Graphitic interlayer states – a carbon *K* near-edge X-ray-absorption fine-structure study. *Physical Review B*, **44**, 1427–1429, https://doi.org/10.1103/PhysRevB.44.1427

Foustoukos, D.I. & Seyfried, W.E., Jr. 2004. Hydrocarbons in hydrothermal vent fluids: the role of chromium-bearing catalysts. *Science*, **304**, 1002–1005, https://doi.org/10.1126/science.1096033

Fralick, P., Davis, D. & Kissin, S.A. 2002. The age of the Gunflint Formation, Ontario, Canada: single zircon U–Pb age determinations from reworked volcanic ash. *Canadian Journal of Earth Sciences*, **39**, 1085–1091, https://doi.org/10.1139/e02-028

French, B. 1964. Graphitization of organic material in a progressively metamorphosed Precambrian iron formation. *Science*, **146**, 917–918, https://doi.org/10.1126/science.146.3646.917

French, B.M. 1971. Stability relations of siderite ($FeCO_3$) in the system Fe–C–O. *American Journal of Science*, **271**, 37–78, https://doi.org/10.2475/ajs.271.1.37

Gérard, E., Moreira, D., Philippot, P., van Kranendonk, M.J. & López-García, P. 2009. Modern subsurface bacteria in pristine 2.7 Ga-old fossil stromatolite drillcore samples from the Fortescue Group, Western Australia. *PLoS One*, **4**, e5298, https://doi.org/10.1371/journal.pone.0005298

Gruner, J.W. 1937. Composition and structure of stilpnomelane. *American Mineralogist*, **22**, 912–925.

Hayes, J.M., Wedeking, W. & Kaplan, I.R. 1983. Precambrian organic geochemistry, preservation of the record. *In*: Schopf, W.J. (ed) *Earth's Earliest Biosphere*. Princeton University Press, Princeton, NJ, 291–301.

Heaney, P.J. & Veblen, D.R. 1991. An examination of spherulitic dubiomicrofossils in Precambrian banded iron formations using the transmission electron microscope. *Precambrian Research*, **49**, 355–372, https://doi.org/10.1016/0301-9268(91)90041-8

Heimann, A., Johnson, C.M., Beard, B.L., Valley, J.W., Roden, E.E., Spicuzza, M.J. & Beukes, N.J. 2010. Fe, C, and O isotope compositions of banded iron formation carbonates demonstrate a major role for dissimilatory iron reduction in 2.5 Ga marine environments. *Earth and Planetary Science Letters*, **294**, 8–18, https://doi.org/10.1016/j.epsl.2010.02.015

Hitchcock, A.P. & Biron, C.E. 1980. Inner-shell excitation of formaldehyde, acetaldehyde, and acetone studied by electron impact. *Journal of Electron Spectroscopy and Related Phenomena*, **19**, 231–250, https://doi.org/10.1016/0368-2048(80)87006-X

Holm, D.K., Schneider, D.A., Rose, S., Mancuso, C., McKenzie, M., Foland, K.A. & Hodges, K.V. 2007. Proterozoic metamorphism and cooling in the southern Lake Superior region, North America and its bearing in crustal evolution. *Precambrian Research*, **157**, 106–126, https://doi.org/10.1016/j.precamres.2007.02.012

Horita, J. 2005. Some perspectives on isotope biosignatures for early life. *Chemical Geology*, **218**, 171–186, https://doi.org/10.1016/j.chemgeo.2005.01.017

House, C.H., Schopf, J.W., McKeegan, K.D., Coath, C.D., Harrison, T.M. & Stetter, K.O. 2000. Carbon isotopic composition of individual Precambrian microfossils. *Geology*, **28**, 707–710, https://doi.org/10.1130/0091-7613(2000)28<707:CICOIP>2.0.CO;2

Ishii, I. & Hitchcook, A.P. 1988. The oscillator strengths for C1*s* and O1*s* excitation of some saturated and unsaturated organic alcohols, acids and esters. *Journal of Electron Spectroscopy and Related Phenomena*, **46**, 55–84, https://doi.org/10.1016/0368-2048(88)80005-7

Jaszczak, J.A., Robinson, G.W., Dimovski, S. & Gogtsi, Y. 2003. Naturally occurring graphite cones. *Carbon*, **41**, 2085–2092, https://doi.org/10.1016/S0008-6223(03)00214-8

Jaszczak, J.A., Dimovski, S. & Hackney, S.A. 2007. Micro- and nanoscale graphite cones and tubes from Hackman Valley, Kola Peninsula, Russia. *Canadian Mineralogist*, **45**, 379–389, https://doi.org/10.2113/gscanmin.45.2.379

Kilcoyne, A.L.D., Tyliszczak, T. *et al.* 2003. Interferometer-controlled scanning transmission X-ray microscopes at the Advanced Light Source. *Journal of Synchrotron Radiation*, **10**, 125–136, https://doi.org/10.1107/S0909049502017739

LaBerge, G.L. 1973 Possible biological origin of Precambrian iron-formations. *Economic Geology*, **68**, 1098–1109.

Lepland, A., Arrhenius, G. & Cornell, D. 2002. Apatite in Early Archean Isua supracrustal rocks in southern West Greenland: its origin, association with graphite and potential as a biomarker. *Precambrian Research*, **118**, 221–241, https://doi.org/10.1016/S0301-9268(02)00106-7

Lepland, A., van Zuilen, M.A. & Philippot, P. 2010. Fluid-deposited graphite and its geobiological implications in early Archean gneiss from Akilia, Greenland. *Geobiology*, **9**, 2–9, https://doi.org/10.1111/j.1472-4669.2010.00261.x

Lepot, K., Williford, K.H., Ushikubo, T., Sugitani, K., Mimura, K., Spicuzza, M. & Valley, J.W. 2013. Texture-specific and isotopic compositions in 3.4 Gyr old organic matter support selective preservation in cell-like structures. *Geochimica et Cosmochimica Acta*, **112**, 66–86, https://doi.org/10.1016/j.gca.2013.03.004

Liu, D., Xu, Y., Papineau, D., Yu, N., Fan, Q., Qiu, X. & Wang, H. 2019. Experimental evidence for abiotic formation of low-temperature proto-dolomite facilitated by clay minerals. *Geochimica et Cosmochimica Acta*, **247**, 83–95, https://doi.org/10.1016/j.gca.2018.12.036

Lougheed, M.S. 1983. Origin of Precambrian iron-formations in the Lake Superior region. *GSA Bulletin*, **94**, 325–340.

Mancuso, J.J., Kneller, W. & Quick, J.C. 1989. Precambrian vein pyrobitumen: Evidence for petroleum generation and migration 2 Ga ago. *Precambrian Research*, **44**, 137–146, https://doi.org/10.1016/0301-9268(89)90079-X

Manning, C.E., Mojzsis, S.J. & Harrison, T.M. 2006. Geology, age and origin of supracrustal rocks at Akilia, West Greenland. *American Journal of Science*, **306**, 1–66, https://doi.org/10.2475/05.2006.02

McCollom, T.M. 2003. Formation of meteorite hydrocarbons from thermal decomposition of siderite ($FeCO_3$). *Geochimica et Cosmochimica Acta*, **67**, 311–317, https://doi.org/10.1016/S0016-7037(02)00945-6

McCollom, T.M. & Seewald, J.S. 2007. Abiotic synthesis of organic compounds in deep-sea hydrothermal environments. *Chemical Reviews*, **107**, 382–401.

McKeegan, K.D., Kudryavtsev, A.B. & Schopf, J.W. 2007. Raman and ion microscopic imagery of graphitic inclusions in apatite from older than 3830 Ma Akilia supracrustal rocks, west Greenland. *Geology*, **35**, 591–594, https://doi.org/10.1130/G23465A.1

Mojzsis, S.J., Arrhenius, G., McKeegan, K.D., Harrison, T.M., Nutman, A.P. & Friend, C.R.L. 1996. Evidence for life on Earth before 3,800 million years ago. *Nature*, **384**, 55–59, https://doi.org/10.1038/384055a0

Mroczkowski, S. & Lichtman, D. 1985. Calculated Auger yields and sensitivity factors for *KLL–NOO* transitions with 1–10 kV primary beams. *Journal of Vacuum Science & Technology A: Vacuum, Surfaces, and Films*, **A3**, 1860–1865, https://doi.org/10.1116/1.572933

Nutman, A.P. 2007. Apatite recrystallisation during prograde metamorphism, Cooma, southeast Australia: implications for using an apatite–graphite association as a biotracer in ancient metasedimentary rocks. *Australian Journal of Earth Sciences*, **54**, 981–990, https://doi.org/10.1080/08120090701488321

Nutman, A.P. & Friend, C.R.L. 2006. Petrography and geochemistry of apatites in banded iron formation, Akilia, W. Greenland: Consequence for oldest life evidence. *Precambrian Research*, **147**, 100–106, https://doi.org/10.1016/j.precamres.2006.02.005

Nutman, A.P., Friend, C.R.L., Bennett, V.C., Wright, D. & Norman, M.D., 2010 >3700 Ma pre-metamorphic dolomite formed by microbial mediation in the Isua supracrustal belt (W. Greenland): Simple evidence for early life?. *Precambrian Research*, **183**, 725–737.

Oehler, D.Z., Robert, F. *et al.* 2009. NanoSIMS: insights to biogenicity and syngeneity of Archaean carbonaceous structures. *Precambrian Research*, **173**, 70–78, https://doi.org/10.1016/j.precamres.2009.01.001

Oehler, D.Z., Robert, F., Walter, M.R., Sugitani, K., Meibom, A., Mostefaoui, S. & Gibson, E.K. 2010. Diversity in the Archean biosphere: new insights from NanoSIMS. *Astrobiology*, **10**, 413–424, https://doi.org/10.1089/ast.2009.0426

Olempska, E. & Wacey, D. 2016. Ambient inclusion trails in Palaeozoic crustaceans (Phosphatocopina and Ostracoda). *Palaeogeography, Palaeoclimatology, Palaeoecology*, **441**, 949–958, https://doi.org/10.1016/j.palaeo.2015.10.052

Papineau, D. 2012. Organic matter associated with apatite in Martian meteorite Chassigny. 43rd Lunar and Planetary Science Conference, p. 1549.

Papineau, D., Purohit, R. *et al.* 2009. High primary productivity and nitrogen cycling after the Paleoproterozoic phosphogenic event in the Aravalli Supergroup, India. *Precambrian Research*, **171**, 37–56, https://doi.org/10.1016/j.precamres.2009.03.005

Papineau, D., DeGregorio, B.T. *et al.* 2010*a*. Ancient graphite in the Eoarchean quartz–pyroxene rock from Akilia in southern West Greenland I: Petrographic and spectroscopic characterization. *Geochimica et Cosmochimica Acta*, **74**, 5862–5883, https://doi.org/10.1016/j.gca.2010.05.025

Papineau, D., DeGregorio, B.T. *et al.* 2010*b*. Ancient graphite in the Eoarchean quartz–pyroxene rock from Akilia in southern West Greenland II: Isotopic and chemical compositions and comparison with Paleoproterozoic banded iron formations. *Geochimica et Cosmochimica Acta*, **74**, 5884–5905, https://doi.org/10.1016/j.gca.2010.07.002

Papineau, D., DeGregorio, B.T., Fearn, S., Kilcoyne, D., McMahon, G., Purohit, R. & Fogel, M.L. 2016. Nanoscale petrographic and geochemical insights on the origin of the Palaeoproterozoic stromatolitic phosphorites from Aravalli Supergroup, India. *Geobiology*, **14**, 3–32, https://doi.org/10.1111/gbi.12164

Papineau, D., She, Z. & Dodd, M.S. 2017. Chemically-oscillating reactions during the diagenetic oxidation of organic matter and in the formation of granules in late Paleoproterozoic chert from Lake Superior. *Chemical Geology*, **47**, 33–54, https://doi.org/10.1016/j.chemgeo.2017.08.021

Pasteris, J.D. 1989. *In situ* analysis in geological thin-sections by laser Raman microprobe spectroscopy: a cautionary note. *Applied Spectroscopy*, **43**, 567–570, https://doi.org/10.1366/0003702894202878

Proskurowski, G., Lilley, M.D. *et al.* 2008. Abiogenic hydrocarbon production at Lost City hydrothermal field. *Science*, **319**, 604–607, https://doi.org/10.1126/science.1151194

Rasmussen, B., Fletcher, I.R., Bekker, A., Muhling, J.R., Gregory, C.J. & Thorne, A.M. 2012. Deposition of 1.88-billion-year-old iron formations as a consequence of rapid crustal growth. *Nature*, **484**, 498–501, https://doi.org/10.1038/nature11021

Rosenberg, R.A., Love, P.J. & Rehn, V. 1986. Polarisation-dependent C(K) near-edge x-ray-absorption fine structure of graphite. *Physical Review B*, **33**, 4034–4037, https://doi.org/10.1103/PhysRevB.33.4034

Roy, S. 2006. Sedimentary manganese metallogenesis in response to the evolution of the Earth system. *Earth-Science Reviews*, **77**, 273–305, https://doi.org/10.1016/j.earscirev.2006.03.004

Rumble, D. 2014. Hydrothermal graphitic carbon. *Elements*, **10**, 427–433, https://doi.org/10.2113/gselements.10.6.427

Rushdi, A.I. & Simoneit, B.R.T. 2004. Condensation reactions and formation of amides, esters, and nitriles under hydrothermal conditions. *Astrobiology*, **4**, 211–224, https://doi.org/10.1089/153110704323175151

Schiffbauer, J.D., Yin, L. *et al.* 2007. Ultrastructural and geochemical characterization of Archean–Paleoproterozoic graphitic particles: implications for recognizing traces of life in highly metamorphosed rocks. *Astrobiology*, **7**, 684–704, https://doi.org/10.1089/ast.2006.0098

Schiffbauer, J.D., Wallace, A.F., Hunter, J.L., Jr., Kowalewski, M., Bodnar, R.J. & Xiao, S. 2012. Thermally-induced structural and chemical alteration of organic-walled microfossils: an experimental approach to understanding fossil preservation in metasediments. *Geobiology*, **10**, 402–423, https://doi.org/10.1111/j.1472-4669.2012.00332.x

Schirmer, M., Walz, M.-M. *et al.* 2011. Electron-beam-induced deposition and post-treatment processes to locally generate clean titanium oxide nanostructures on Si (100). *Nanotechnology*, **22**, 085301, https://doi.org/10.1088/0957-4484/22/8/085301

Schneider, D.A., Bickford, M.E., Cannon, W.F., Schulz, K.J. & Hamilton, M.A. 2002. Age of volcanic rocks and syndepositional iron formations, Marquette Range Supergroup: implications for the tectonic setting of Paleoproterozoic iron formations of the Lake Superior region. *Canadian Journal of Earth Sciences*, **39**, 999–1012, https://doi.org/10.1139/e02-016

Schoonen, M.A.A. & Xu, Y. 2001. Nitrogen reduction under hydrothermal vent conditions: implications for the prebiotic synthesis of C–H–O–N compounds. *Astrobiology*, **1**, 133–142, https://doi.org/10.1089/153110701753198909

Schulz, K.J. & Cannon, W.F. 2007. The Penokean orogeny in the Lake Superior region. *Precambrian Research*, **157**, 4–25, https://doi.org/10.1016/j.precamres.2007.02.022

Schwab, V., Spangenberg, J.E. & Grimalt, J.O. 2005. Chemical and carbon isotopic evolution of hydrocarbons during prograde metamorphism from 100°C to 500°C: case study in the Liassic black shale formation of Central Swiss Alps. *Geochimica et Cosmochimica Acta*, **69**, 1825–1840, https://doi.org/10.1016/j.gca.2004.09.011

Shapiro, R.S. & Konhauser, K.O. 2015. Hematite-coated microfossils: primary ecological fingerprint or taphonomic oddity of the Paleoproterozoic? *Geobiology*, **13**, 209–224, https://doi.org/10.1111/gbi.12127

Smirnov, A., Hausner, D., Laffers, R., Strongin, D.R. & Schoonen, M.A.A. 2008. Abiotic ammonium formation in the presence of Ni–Fe metals and alloys and its implication for the Hadean nitrogen cycle. *Geochemical Transactions*, **9**, https://doi.org/10.1186/1467-4866-9-5

Steele, A., McCubbin, F.M. *et al.* 2012. A reduced organic carbon component in Martian basalts. *Science*, **337**, 212–215, https://doi.org/10.1126/science.1220715

Summers, D.P. & Chang, S. 1993. Prebiotic ammonia from reduction of nitrite by iron (II) on the early Earth. *Nature*, **365**, 630–633, https://doi.org/10.1038/365630a0

Tan, S., Livengood, R., Hack, P., Hallstein, R. & Shima, D. 2010. Nanomachining with a focused neon beam: A preliminary investigation for semiconductor circuit editing as failure analysis. *Journal of Vacuum Science & Technology B: Microelectronics and Nanometer Structures*, **29**, 06F604-601, https://doi.org/10.1116/1.3660797

Vandenbroucke, M. & Largeau, C. 2007. Kerogen origin, evolution and structure. *Organic Geochemistry*, **38**, 719–833, https://doi.org/10.1016/j.orggeochem.2007.01.001

Van Wyck, N. & Johnson, C.M. 1997. Common lead, Sm–Nd, and U–Pb constraints on petrogenesis, crustal architecture and tectonic setting of the Penokean orogeny (Paleoproterozoic) in Wisconsin. *Geological Society of America Bulletin*, **109**, 799–808, https://doi.org/10.1130/0016-7606(1997)109<0799:CLSNAU>2.3.CO;2

Wacey, D., Menon, S. *et al.* 2012. Taphonomy of very ancient microfossils from the 3400 Ma Strelley Pool Formation and 1900 Ma Gunflint Formation: New insights using a focused ion beam. *Precambrian Research*, **220–221**, 234–250, https://doi.org/10.1016/j.precamres.2012.08.005

Wacey, D., McLoughlin, N., Kilburn, M.R., Saunders, M., Cliff, J.B. & Kong, C. 2013. Nanoscale analysis of pyritized microfossils reveals differential heterotrophic consumption in the ~1.9 Ga Gunflint chert. *Proceedings of the National Academy of Sciences of the USA*, **110**, 8020–8024, https://doi.org/10.1073/pnas.1221965110

Watanabe, Y., Naraoka, H., Wronkiewicz, D.J., Condie, K.C. & Ohmoto, H. 1997. Carbon, nitrogen and sulphur geochemistry of Archean and Proterozoic shales from the Kaapvaal Craton, South Africa. *Geochimica et Cosmochimica Acta*, **61**, 3441–3459, https://doi.org/10.1016/S0016-7037(97)00164-6

Williford, K.H., Ushikubo, T., Schopf, J.W., Lepot, K., Kitajima, K. & Valley, J.W. 2013. Preservation and detection of microstructural and taxonomic correlations in the carbon isotopic compositions of individual Precambrian microfossils. *Geochimica et Cosmochimica Acta*, **104**, 165–182, https://doi.org/10.1016/j.gca.2012.11.005

Williford, K.H., Ushikubo, T. *et al.* 2015. Carbon and sulfur isotopic signatures of ancient life and environment at the microbial scale: Neoarchean shales and carbonates. *Geobiology*, https://doi.org/10.1111/gbi.12163

Winter, B.L. & Knauth, L.P. 1992. Stable isotope geochemistry of cherts and carbonates from the 2.0 Ga Gunflint iron formation: implications for the depositional setting, and the effects of diagenesis and metamorphism. *Precambrian Research*, **59**, 283–313, https://doi.org/10.1016/0301-9268(92)90061-R

Wirth, R. 2009. Focused Ion Beam (FIB) combined with SEM and TEM: Advanced analytical tools for studies of chemical composition, microstructure and crystal structure in geomaterials on a nanometer scale. *Chemical Geology*, **261**, 217–229, https://doi.org/10.1016/j.chemgeo.2008.05.019